제한된 미세채널 유동에서의

브라운 입자 거동에 관한 수치모사 연구

Numerical study on the dynamics of Brownian particulate

systems in confined microchannel flow

지도교수 이 승 종

이 논문을 공학박사 학위논문으로 제출함

2014년 5월

서울대학교 대학원

화학생물공학부
최 성 업

Abstract

Numerical study on the dynamics of

Brownian particulate systems

in confined microchannel flow

Sungup Choi

School of Chemical and Biological Engineering

The Graduate School

Seoul National University

The numerical study on particulate systems in confined microchannel flow is significantly important in developing lab-on-a-chip devices for various applications and accordingly, this aspect has attracted much attention in fundamental and applied research. Firstly, we have investigated the dynamics of short double-stranded DNA molecules which

move through a deep–shallow alternating nanofilter with Brownian dynamics simulation. We proposed a novel mechanism for high-throughput DNA separation with a high electric field, which was originally predicted by Laachi *et al.* (Physical Review Letters, 2007, 98). In this work, we show that DNA molecules deterministically move along different electrophoretic streamlines according to their length, owing to geometric constraint at the exit of the shallow region. Consequently, it is more probable that long DNA molecules pass over a deep well region without significant lateral migration toward the bottom of the deep well, which is in contrast to the long dwelling time for short DNA molecules. We investigated the dynamics of DNA passage through a nanofilter facilitating electrophoretic field kinematics. The statistical distribution of the DNA molecules according to their size clearly corroborates our assumption. On the other hand, it was also found that the tapering angle between the shallow and deep regions significantly affects the DNA separation performance. The current results show that the non-uniform field effect combined with geometric constraint plays a key role in nanofilter-based DNA separation. We expect that our results will be helpful in designing and operating nanofluidics-based DNA separation devices and in understanding the polymer dynamics in confined geometries.

In addition, the dynamics of complex fluids in confined complex

geometry have been investigated to observe the microstructural change and its interaction with flow. To understand the characteristics of these complex flows, we have studied the dynamics of aggregating particle suspensions in three dimensional 4:1 contraction flow using the self-consistent particle simulation method. It combines both Brownian dynamics and finite element methods self-consistently, which enables to consider long-range hydrodynamic interaction effectively. We observed heterogeneous cluster formation and analyzed it in terms of the competition between flow and interparticle forces. In addition, spatio-temporal fluctuation which originates from the microstructural change and its interaction with the flow was observed. The fluctuation was complex with no characteristic periodicity or pattern. Heterogeneous structure formation and spatio-temporal fluctuation were found to be the main factors that characterize the complex flow of the particulate suspensions in the micro-contraction channel flow.

Student Number: 2004-23538

Contents

List of Figures

xiii

Chapter 1. Introduction

1.1. Background on particle suspensions in confined microc hannel flow

The complex flow of particle suspensions [Bernate *et al*. (2012), Desreumaux *et al*. (2013), Sengupta *et al*. (2013), Gachelin *et al*. (2013)] in confined geometry such as micro-fabricated device has drawn much attention in recent years. It provides a useful platform in developing lab-on-a-chip devices for various applications such as mixing [Wootton *et al*. 2012], separation [Meinhardt *et al*. (2012), Reguera *et al*. (2012)], medical diagnostics [Utz *et al*. (2010)], to list a few.

DNA separation using electrophoretic motion in confined micro/nano-fabricated channel has drawn much attention for some decades. One of them, micro-/nanofabrication approaches, nanofilter separation [Fu *et al*. (2005), Fu *et al*. (2006)] with periodically alternating deep and shallow regions. The dynamics of DNA separation has been studied experimentally [Viovy (2000)] and Dorfman [Dorfman (2010), Doyle *et al*. (2002), Fu *et al*. (2005), Fu *et al*. (2006), Dorfman *et al*. (2013)] and numerically [Laachi *et*

al. (2007)], but inherent deterministic dynamics of short double-strand DNA (dsDNA) molecule by electric field kinematics in high throughput regime is non-negligible. Thus, we deal with the constraint effect between DNA molecule and confined nanofilter arrays by Browinian dynamics (BD) in this work.

The complexities of particulate suspension flow has also showed interesting behaviors such as crystallization [Wu *et al.* (2009), Shereda *et al.* (2010)[1], Shereda *et al.* (2010)[2]], flow induced ordering [Chen *et al.* (1994), Loose *et al.* (1994), Stancik *et al.* (2004)], particle transport due to confinement effect [Karlsson *et al.* (2002), Schwierz *et al.* (2010)], flow instability [Isa *et al.* (2009)], and so on. However, characteristic of paraticulate suspension flow in complex geometry is almost unknown field for difficulties of flow control and observation. However, it is now possible to approach the unknown field of particulate suspension in complex geometry numerically because self-consistent particle simulation technique (SC) [Myung *et al.* (2011)] was developed [Myung *et al.* (2011)]. By adopting SC method, we investigated the dynamics of aggregating particulate suspensions in the microchannel flow of 4:1 planar contraction.

1.2. DNA separation mechanism in nanofilter arrays

DNA separation on the basis on molecular size is an essential step in genome sequencing and mapping, and gel electrophoresis has been a standard method for DNA separation [Viovy (2000)]. However, the inherent non-uniformity in pore size and shape in a gel can deteriorate the DNA separation performance [Viovy (2000)]. In the last decades, several studies have been conducted to overcome the disadvantages of conventional gel electrophoresis [Viovy (2000)]. Among such approaches, separation devices based on micro-/nanofabrication have attracted much attention [Austin *et al*. (1993), Nixon *et al*. (1994), Sevick *et al*. (1994)[1], Sevick *et al*. (1994)[2], Volkmuth *et al*. (1994), Saville *et al*. (1996), Duke *et al*. (1998), Bakajin *et al*. (2001), Doyle *et al*. (2002), Minc *et al*. (2004), Fu *et al*. (2005), Fu *et al*. (2006)] For instance, obstacle arrays based on DNA hooking collision [Austin *et al*. (1993), Nixon *et al*. (1994), Sevick *et al*. (1994)[1], Sevick *et al*. (1994)[2], Volkmuth *et al*. (1994), Saville *et al*. (1996), Bakajin *et al*. (2001), Doyle *et al*. (2002), Minc *et al*. (2004)] and diffusion-based arrays [Duke *et al*. (1998)] have been exploited in DNA separation. Among these micro-/nanofabrication approaches, nanofilter separation [Fu *et al*. (2005), Fu *et al*. (2006)] with periodically alternating deep and shallow regions [refer to

Fig.1.1] has been
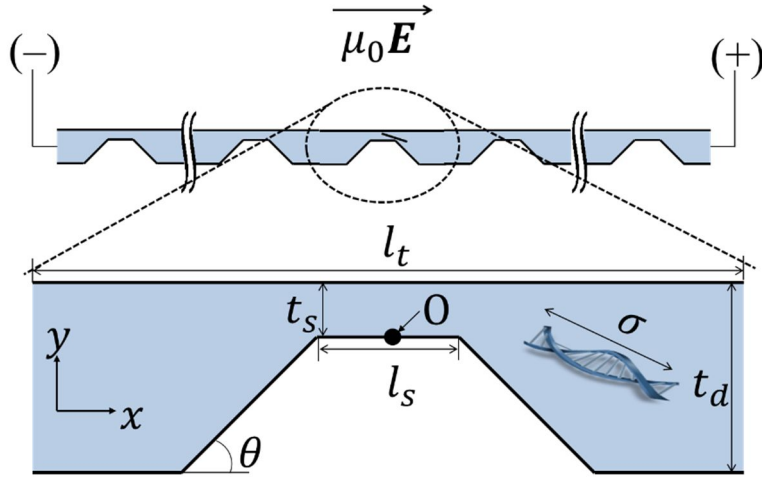
Fig. 1.1. Schematic design of a periodic nanofilter channel (upper panel) and enlargement of a unit nanofilter channel (lower panel), where l_t and l_s are the lengths of total channel and shallow slit in unit channel, respectively. t_s and t_d are the thicknesses of the shallow slit and deep well; σ is the length of the DNA molecule, and φ is the angle formed between the backbone of the DNA and the net electric field direction.

considered to be a promising tool. It has been demonstrated that this method can be utilized for a wide range of DNA molecular weights (M.W.), i.e., 10 bp < M.W. < 100 kbp, and the thicknesses of the deep (t_d) and shallow (t_s) regions can be changed depending on the target-DNA molecular weight [Fu *et al*. (2005), Fu *et al*. (2006)]. The DNA mobility in nanofilter arrays has been shown to be dramatically higher than that in typical gel-based electrophoresis, which guarantees a high-throughput separation performance. Furthermore, the technique has also been successfully integrated into miniaturized lab-on-a-chip devices [Doyle *et al*. (2002), Fu *et al*. (2005), Fu *et al*. (2006)].

The DNA separation mechanism in nanofilter arrays can be categorized into different mechanisms according to the relative ratio of DNA size to t_s, where the DNA size is typically represented by the radius of gyration, R_g. Briefly, Ogston sieving and entropic trapping mechanisms are applied for $R_g/t_s < 1$ and $R_g/t_s > 1$, respectively. Further details on these mechanisms are described in review papers by Viovy [Viovy (2000)] and Dorfman [Dorfman (2010), Dorfman *et al*. (2013)]. In the present work, we focused on the separation of relatively small DNA molecules compared to t_s and thus, our interest is limited to the so-called Ogston sieving regime. In the

Ogston sieving regime, the steric hindrance interaction between a DNA molecule and the channel wall is an important factor for the size-dependent mobility difference [Viovy (2000)]. There have been several experimental studies [Fu *et al*. (2005), Fu *et al*. (2006), Fu *et al*. (2007)] on short double-strand DNA (dsDNA) molecules for which the DNA length (σ) is comparable to the thickness of the shallow slit (e.g., both σ and $t_s \sim 100$ nm). In this regime, shorter DNA molecules are expected to pass through the nanofilter arrays more rapidly than the longer DNA molecules [Fu *et al*. (2006)].

Laachi et al. [Laachi *et al*. (2007)] assumed dsDNA to be a rod-like polymer because its length is comparable to the DNA persistence length ($l_p \sim 50$ nm). They investigated the dynamics and separation mechanism of the short rod-like DNA molecules in the Ogston sieving regime, by utilizing Brownian dynamics (BD) simulations. Interestingly, with a high electric field, they predicted that relatively longer DNA chains will pass more quickly through the nanofilter than shorter DNA chains, which was contrary to our intuition. They proposed that this phenomenon can be considered to be a novel high-throughput DNA separation mechanism explained that the torque assisted-rotation of the DNA molecules at the entrance of the shallow region is responsible for the high-throughput DNA separation, in which the torque is

proportional to the DNA length, i.e., long DNA molecules are more easily aligned than short DNA molecules along the longitudinal direction of the shallow region, and consequently, long DNA enters more quickly into the shallow region [Laachi *et al*. (2007)]. Later, this high-throughput separation mechanism was experimentally observed [Fu *et al*. (2005), Strychalski *et al*. (2009)]. However, at higher electric fields, this high-throughput separation mechanism broke down, which was attributed to non-negligible DNA bending under the high electric field [Strychalski *et al*. (2009), Fayad *et al*. (2010)].

In this work, we propose a novel mechanism for high-throughput DNA separation within a high electric field regime. We found that the geometrical constraint significantly affects the lateral motion of the DNA molecules when a DNA leaves the shallow region. Our proposed mechanism is analogous to the "deterministic lateral displacement" for DNA separation with bumped arrays [Huang *et al*. (2004)], where DNA molecules follow different streamlines according to their size. In this work, the geometric constraint effect was systematically analyzed with field kinematics that was numerically predicted with the finite element method (FEM) and the ensemble-averaged passage time of DNA molecules was calculated based on BD simulation. In addition, we investigated how the tapering angle between

the deep and shallow regions (θ) [Fig. 1.1] influenced the DNA separation performance, which can be useful for further optimization of the channel design and operation conditions.

1.3. Aggregating particle under 4:1 planar contraction channel flow

The flow of particle systems in confined microchannel showed interesting behaviors and their complexities such as crystallization [Wu *et al*. (2009), Shereda *et al*. (2010)[1], Shereda *et al*. (2010)[2]], flow induced ordering [Chen *et al*. (1994), Loose *et al*. (1994), Stancik *et al*. (2004)], particle transport [Karlsson *et al*. (2002), Schwierz *et al*. (2010)] and flow instability [Isa *et al*. (2009)] have been studied in many groups.

However, most of these studies focused on the dynamics in simple shear flow due to the difficulties in the control of complex flow. On the other hand, the flow characteristics which involves complex flow such as curve, contraction, expansion, and others are rarely understood. The experimental studies on the flow of particle systems under complex flow field have difficulties in the visualization and in the control of complex flows so that the numerical simulation needs to be applied for these systems. Brownian

Dynamics (BD) [Mitchell *et al*. (1995), Strating (1999), Foss *et al*. (2000), Schwierz *et al*. (2010)] is one of the simplest methods for particulate flows. However, it does not consider hydrodynamic interaction (HI). Stokesian Dynamics (SD) [Brady *et al*. (1998), Foss *et al*. (2000)] realizes the hydrodynamic interaction precisely. However, it requires massive computational resources and has limitation in the application to complex flows. Mesoscale simulations [Rotall *et al*. (2007), Pan *et al*. (2010)] reproduce the hydrodynamic interaction efficiently, but they also require large computational power and the number of particles they can cover is limited.

To overcome these difficulties, self-consistent particle simulation technique (SC) [Myung *et al*. (2011)] was developed. SC adopts the concept of the micro-macro simulation method [Laso *et al*. (1993), Hulsen *et al*. (1997), Wapperom *et al*. (2000)] which takes into account the interaction between flow and polymer configuration. The SC method is particularly appropriate for the study of particle systems under complex flow field because it solves the complex flow field directly in the finite elements. We applied the SC method to three dimensional 4:1 planar contraction flow. This flow has been widely studied in experiments [Nguyen *et al*. (1979), Mckinley *et al*. (1991), Feigl *et al*. (1994)] and has also been regarded as a

benchmarking problem in numerical simulation [Crochet *et al*. (1984), Kim *et al*. (2005), Kwon *et al*. (2012)]. Thanks to recent increase in computational power and advances in numerical algorithm, we could investigate the particle flows in 3D micro-contraction channel. The contraction flow of the particle system showed a strong spatio-temporal fluctuation, which was related to the microstructural change and its interaction with flow. The results will contribute to our understanding on the complex flow behavior of many-body particle systems in the microchannel flow and to possible applications in high end technologies.

Chapter 2. Theory

2.1. Dynamics of DNA molecule through electrophoretic field kinematics

We briefly summarize the background theories on short rod-like DNA transportation through deep-shallow alternating nanofilter [Laachi *et al*. (2007)]. The length of the DNA molecule was typically less than 100 nm ($\sim 2l_p$), and it was regarded as a rod-like polymer [Laachi *et al*. (2007)]. In the current work, the DNA length was longer than the thickness of the shallow region ($\sigma > t_s$) [Fig. 1.1]. Therefore, a DNA molecule should be aligned along the longitudinal direction of the shallow region so that the

molecules can enter the shallow region. Under weak electric fields, shorter molecules enter and leave the shallow region faster than longer molecules do, according to the so-called Ogston sieving mechanism [Laachi *et al*. (2007)]. In this regime, a shorter molecule is more favorable in satisfying the geometric constraint ($|\varphi| < \varphi_{\max}$, $\varphi_{\max} = \sin^{-1}(t_s / \sigma)$, $\varphi = \cos^{-1}(|\hat{\sigma} \cdot \hat{e}_x|)$, where $\hat{\sigma}$ and $\hat{e}_x$ are the unit vectors of the rod and the longitudinal direction of the unit channel, respectively), because the allowable rotational angle to enter the shallow channel $\varphi_{\max}$ becomes broader as the molecular size σ decreases [Laachi *et al*. (2007)]. Furthermore, the rotational diffusion time [Broersma (1960)[1], Broersma (1960)[2], Yamakawa (1971), Berne *et al*. (1976), Newman *et al*. (1977)] decreases with decreasing σ ($t_{\text{rotation}} \sim \sigma^3 / \log \sigma$), and the rotation time of the molecule satisfying the constraint is shorter with a decreasing σ. Taken together, it is expected that short DNA molecules will be more favorably aligned than long DNA molecules along the longitudinal direction of the shallow region.

On the other hand, it was predicted that at a high electric field, long molecules anomalously leave the nanofilter more quickly than short molecules do [Laachi *et al*. (2007)]. In this regime, the alignment of a DNA molecule along the longitudinal direction, i.e., a favorable DNA

conformation to enter the shallow region, is driven by the rotational torque of the DNA molecules (M : $|M| \propto \sigma^2$) [Laachi *et al*. (2007)]. This torque is induced by a non-homogeneous electric field at the entrance region of the shallow region, and the DNA separation based on the size-dependent rotational torque was termed "torque-assisted separation mechanism" [Laachi *et al*. (2007)]. Although, it is expected that the high-throughput DNA separation eventually deteriorates at further higher electric fields because the initialization (or randomization) of the DNA conformation by rotational diffusion is a prerequisite for the "torque-assisted separation mechanism" [Laachi *et al*. (2007)]. However, at extremely high electric fields, the DNA molecules will transit from one shallow region to another without conformational change. This reduction in DNA separation resolution was not observed in the BD simulation [Laachi *et al*. (2007)].

In addition, it is not well understood how the geometric constraint near the exit of the shallow region affects the DNA separation. As shown in Fig. 2.1, a rod-like polymer is modeled as a dumbbell composed of two beads connected with a rod (the detailed description for numerical modeling is presented in the next section), and the dynamics of a dumbbell at the exit is expected to be greatly affected by the wall constraint. For simplicity, we assume that each bead deterministically moves along the electrophoretic

streamlines at each bead's location (the electrophoretic streamlines are represented as color contours in Fig 2.1), and this condition corresponds to DNA dynamics under extremely high electric fields, in which Brownian motion is not relevant. For instance, we can consider that the fore and aft beads follow the streamlines between the bottom and upper walls inside the shallow
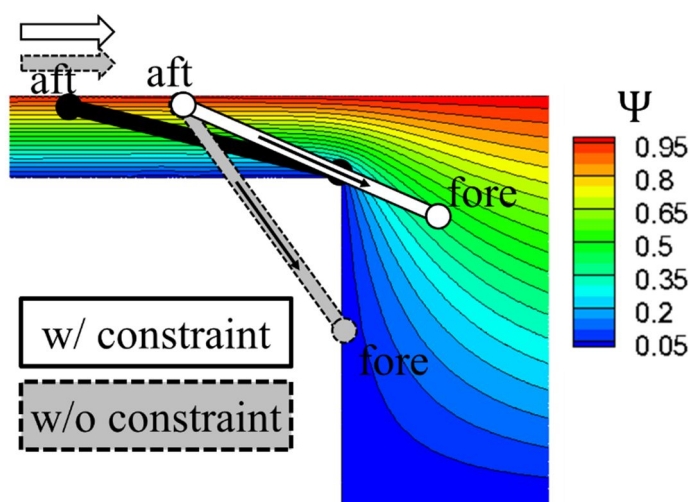
Fig. 2.1. Schematic representation of a molecule leaving the shallow slit with (*white*) and without (*gray*) the constraint effect.

regions [*black* dumbbell in Fig. 2.1]. The wall penetration of a rod is physically prohibited [*gray* dumbbell in Fig. 2.1]. Thus, the final location of a fore bead is greatly influenced by the rod constraint: a fore bead is impelled by an aft bead continuously, and thus, the fore bead reaches the end of a streamline that is quite distant from the bottom wall [un-filled dumbbell in Fig. 2.1]. Consequently, it is anticipated that the distance between the centroid of longer DNA molecules and the upper wall is less than that between the centroid of shorter DNA molecules and the upper wall. Thus, long DNA molecules reach the next shallow region by following trajectories shorter than those followed by short DNA molecules. We note that the centroid shift of DNA molecules toward the upper wall does not occur when the fore and aft beads move along the upper and bottom walls, respectively. In this case, each bead constantly follows the same streamline until the aft bead leaves the shallow region, and the centroid streamline is that of the mid-

point between the upper and bottom walls irrespective of the DNA molecule size [Fig. 2.2].

The centroid shift toward the upper wall is observed in the distribution of dwelling time at each position as shown in Fig. 2.3. We consider a specific case for the transportation of a cylindrical rod-like DNA molecule with length σ and radius a ($\sigma = 4.00 t_s$ and $a = 1\,\mathrm{nm}$) in an electrolyte solution with
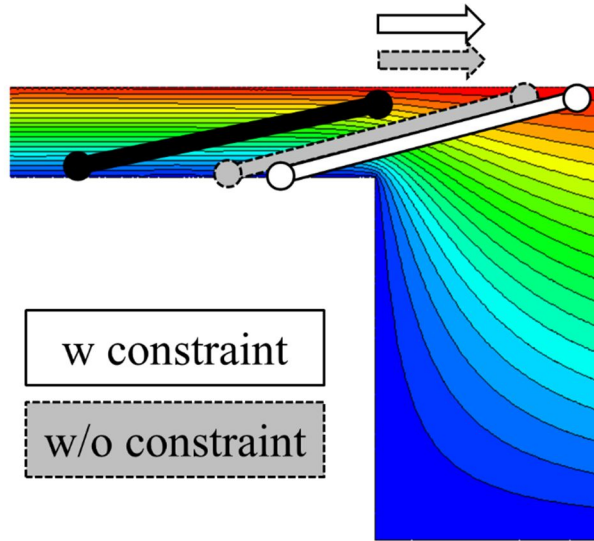
Fig. 2.2. Schematic procedure of molecule exiting shallow slit with (*white*) and without (*gray*) constraint effect when its rotational angle is positive.
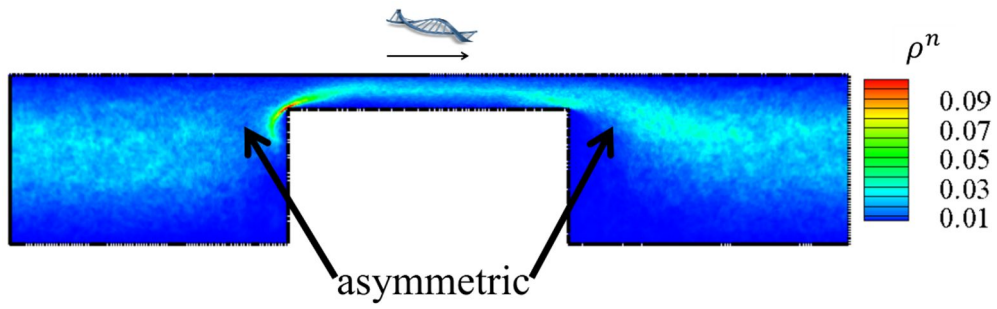
Fig. 2.3. Distribution probability of the centroid of the molecule when $\sigma / t_s = 4.00$, $Pe^b = 10$.

electrophoretic   mobility, μ_0 ,   and   solvent   viscosity η_s

($\mu_0 \sim 10^{-4}$ cm^2/V·s, $\eta_s \sim 10^{-3}$ Pa·s) in a nanofilter channel geometry

($\alpha = 1/3$ and $\delta = 1/5$, where $\alpha = l_s/l_t$, $\delta = t_s/t_d$) under an electric field

E_{av} of ~3000 V/cm; here, E_{av} is the averaged electric field strength over a

single nanofilter unit and is defined as $\Delta V/l_t$, and ΔV is the electric

potential difference between the inlet and outlet for a nanofilter unit. We note

that E_{av} considered in this estimation is stronger than that under practical

separation conditions. At a higher electric field, the dynamics of rod-like

molecule in a filtration process in a nanofilter channel is more deterministic

than that in a low-electric-field case, which follows the "deterministic lateral

displacement" mechanism [Huang *et al.* (2004)] in which the DNA

molecules follow different streamlines according to their size.

Fig. 2.3 shows the probability of dwelling time over the entire filtration process. The dwelling time distribution is asymmetric: the dwelling probability is lower near the corner encountered just after a shallow slit than at the corner before the shallow slit. This observation corroborates our assumption that the geometric constraint significantly affects the lateral distribution of the molecules just after the shallow slot, and thus, the molecules move along different electrophoretic streamlines depending on their size.

Further, we analyzed the time scales required in the diffusional and translational convectional motions in deep well to investigate the molecular dynamics within the high-throughput regime. The compared time scales were quantitatively analyzed with the relative ratios of the free translational (in lateral direction) or rotational diffusion time ($\tau_{d,t}$ or $\tau_{d,r}$) to the electrophoretic convection time in the deep well part ($\tau_{e,d}$), respectively. $\tau_{d,t}$ is the translational diffusion time defined as σ^2 / D_t and $\tau_{d,r}$ is the rotational diffusion time defined as $\varphi_{\max} / D_r$, where D_t and D_r are the translational and rotational diffusion coefficients, respectively, at infinite dilution determined by employing the Broersma theory [Broersma (1960)[1], Broersma (1960)[2], Yamakawa (1971), Zero *et al.* (1981)]. The translational

diffusion coefficient D_t of a rigid cylindrical rod is predicted as follows [Broersma (1960)[1], Broersma (1960)[2], Yamakawa (1971), Zero *et al.* (1981)]:

$$D_t = k_B T / 3\pi\eta_s\sigma[\lambda - 0.5(\gamma_\parallel + \gamma_\perp)], \tag{1}$$

where k_B is the Boltzmann constant, T is the absolute temperature, λ is the logarithmic aspect ratio of σ to a, and $\gamma_\parallel$ and $\gamma_\perp$ are the translational friction coefficients for motions parallel and perpendicular to the axis of the rod [$\gamma_\parallel = 1.27 - 7.4(1/\lambda - 0.34)^2$, and $\gamma_\perp = 0.19 - 4.2(1/\lambda - 0.39)^2$] [Broersma (1960)[1], Broersma (1960)[2]]. The rotational diffusion coefficient D_r is predicted as follows: [Broersma (1960)[1], Broersma (1960)[2], Yamakawa (1971), Zero *et al.* (1981)]

$$D_r = 3k_B T / \pi\eta_s(\lambda - \xi), \tag{2}$$

where ξ denotes a fitting parameter [$\xi = 1.45 - 7.5(1/\lambda - 0.27)^2$] [Broersma (1960)[1], Broersma (1960)[2]]. $\tau_{e,d}$ is the electrophoretic convection time in a deep well, which is expressed as follows:

$$\tau_{e,d} = (l_t - l_s) / \mu_0 E_d, \tag{3}$$

where the electric field strength in a deep well E_d is predicted as $E_d = \delta E_{av} / [\alpha + \delta(1-\alpha)]$.

We consider a specific case for the transportation of a rod-like DNA

molecule with the same conditions in Fig. 2.3. For this case, the predicted ratio of $\tau_{d,t}/\tau_{e,d}$ is about 15, and thus, the electrophoretic convective time scale across the deep well is too short for the molecule to diffuse far into a deep well. On the other hand, $\tau_{d,r}/\tau_{e,d}$ is about 0.075, which indicates sufficient time for a molecule's rotational angle $|\varphi|$ to become larger than φ_{max} in a deep well, which is an imperative for the electro-torque-assisted DNA separation mechanism (or high-throughput separation mechanism). However, the rotation of a DNA molecule is available only when the molecule is sufficiently far from the wall, but the slow translational diffusion (in the lateral direction) limits the free rotation because $\tau_{d,t}/\tau_{e,d}$ is only ~15, as discussed above. Moreover, due to the centroid shift to the upper wall after the shallow slit, significant portions of long molecules deterministically move along electrophoretic streamlines close to the upper wall where the rotational motion is restricted. Therefore, we assume that the "torque-assisted separation mechanism" [Laachi *et al.* (2007)] is not the only mechanism for the high-throughput process. In addition, the "torque-assisted separation mechanism" inherently assumes that the dwelling time, near the entrance region of the shallow slit, depends upon the rod length, and this dependency plays a key role in size-based DNA separation. We investigated

the spatial distribution of the molecules within the nanofilter in order to reveal whether the assumption is relevant.

2.2. Self-consistent particle simulation method

The SC method is divided into two parts. The first part involves Brownian dynamics (BD) which solves the motion of the particles. The second part calculates the flow field by solving the conservation equation of momentum and mass, using the finite element method (FEM) [Crochet *et al*. (1984)]. The flow-particle interaction in each finite element E is considered via particle stress which works as an external stress such that SC takes the long-range interaction between the particle and fluid (but not the lubrication force) into account [Myung *et al*. (2011), Myung *et al*. (2013)]. Calculation of the two parts was conducted alternatively and repeatedly sharing the particle stress and velocity field obtained in BD and FEM step respectively as schematically represented in Fig. 2.4.

BD (particle)

$$dr_i / dt = \boldsymbol{u}_i^m (\boldsymbol{r}_i) + 1/\varsigma \left(F_i^P + F_i^B \right)$$

$$\boldsymbol{\tau}_p = -1/V^E \left\langle \boldsymbol{r}_{ij} \boldsymbol{F}_{ij}^P \right\rangle$$

$$\boldsymbol{u}^m$$

FEM (flow)

$$0 = -\nabla p + \eta \nabla^2 \boldsymbol{u}^m + \nabla \cdot \boldsymbol{\tau}_p$$

$$0 = \nabla \cdot \boldsymbol{u}^m$$
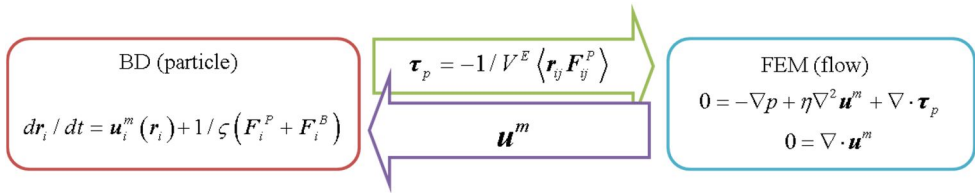
Fig. 2.4. Schematic representation of Self-consitent particle simulation algorithm

2.2.1. Dynamics of spherical particle (Brownian dynamics)

The position of ith particle $\boldsymbol{r}_i$ is governed by the hydrodynamic force ($\boldsymbol{F}_i^H$), the Brownian force ($\boldsymbol{F}_i^B$) and the potential force ($\boldsymbol{F}_i^P$),

$$md^2\boldsymbol{r}_i / dt^2 = \boldsymbol{F}_i^H + \boldsymbol{F}_i^B + \boldsymbol{F}_i^P, \tag{4}$$

where m is the mass of the particle. If time step is long enough to relax the momentum of the particles, the inertia term can be neglected. The many-body hydrodynamic interaction was neglected and the hydrodynamic force ($\boldsymbol{F}_i^H$) was simplified as,

$$\boldsymbol{F}_i^H = -\varsigma[d\boldsymbol{r}_i / dt - \boldsymbol{u}_i^m(\boldsymbol{r}_i)], \tag{5}$$

where $\boldsymbol{u}_i^m(\boldsymbol{r}_i)$ is the flow field of the medium at the position $\boldsymbol{r}_i$ and ς is the friction coefficient. The Brownian force ($\boldsymbol{F}_i^B$) is related to the random motion of the particles generated by the collision with surrounding solvent

molecules. In the modeling, $\boldsymbol{F}_i^B$ was assigned as random such that it has

zero mean and variance of $2k_BT\varsigma$ [Öttinger (1996)],

$$< \boldsymbol{F}_i^B(t) >= 0 \tag{6}$$

$$< \boldsymbol{F}_i^B(t)\boldsymbol{F}_j^B(t') >= 2k_BT\varsigma\delta_{ij}\delta(t-t')\boldsymbol{\delta}, \tag{7}$$

where k_B the is Boltzmann's constant and T is the absolute temperature.

The potential force $\boldsymbol{F}_i^P$ is expressed as $\boldsymbol{F}_i^P = \sum_j \boldsymbol{F}_{ij}^P$, where $\boldsymbol{F}_{ij}^P$ is the

interparticle potential force between the particles i and j which is

calculated from the negative gradient of the potential curve.

2.2.2. Calculation of flow field (Finite element method)

The second part calculates flow field by solving the conservation equation of momentum and mass,

$$0 = -\nabla p + \eta \nabla^2 \boldsymbol{u}^m + \nabla \cdot \boldsymbol{\tau}_p \tag{8}$$

$$\nabla \cdot \boldsymbol{u}^m = 0, \tag{9}$$

where p is the pressure, η is the medium viscosity and $\boldsymbol{\tau}_p$ is the particle stress. The particle stress ($\boldsymbol{\tau}_p$) is the stress contribution from the particles, as an extra stress term in the momentum balance equation. The particle stress in a finite element E is defined as,

$$\boldsymbol{\tau}_p^E = -\frac{1}{V^E} \sum_{i=1}^{N_p-1} \sum_{j=i+1}^{N_p} \boldsymbol{r}_{ij} \boldsymbol{F}_{ij}^P, \tag{10}$$

where V^E is the volume of the element E and N_P is the number of particles belonging to the element. The nodal particle stress is defined as

$$\boldsymbol{\tau}_p^n = -\frac{\sum_{i=1}^{N_E} V^{E_i} \boldsymbol{\tau}_p^{E_i}}{\sum_{i=1}^{N_E} V^{E_i}}, \qquad (11)$$

where N_E is the number of elements sharing the node. The stress and pressure were non-dimensionalized by the characteristic values of $k_B T / a^3$ such that Eq. (8) and (9) are non-dimensionalized as

$$0 = -\nabla \tilde{p} + 1 / 6\pi \nabla^2 \tilde{\boldsymbol{u}}^m + \nabla \cdot \tilde{\boldsymbol{\tau}}_p \qquad (12)$$

$$\nabla \cdot \tilde{\boldsymbol{u}}^m = 0 \qquad (13)$$

The velocity and pressure are computed with standard Galerkin finite element method [Crochet *et al*. (1984)], where $\boldsymbol{u}^m$ is interpolated with 27-node biquadratic shape function (P_2^1) and the pressure and stress are interpolated with 8-node bilinear shape function (P_1^0).

Chapter 3. DNA Separation in Nanofilter Arrays

3.1. Numerical methods

3.1.1. Dynamics of rigid dumbbell (Brownian dynamics)

In this work, we investigated the dynamics of short DNA molecules by using BD simulation and adopted a dumbbell model to describe a rod-like polymer, which consisted of two-beads connected by a rod. The evolution equation for each bead location (r_i^b) is presented as follows:

$$dr_i^b \,/\, dt = \mu_0 E(r_i^b) + 1/\varsigma^b (F_i^B + F_i^C), \qquad (14)$$

where μ_0 is assumed as independent of the molecular size, and $E(r_i^b)$ is the local electric field at the bead location, r_i^b. The frictional coefficient of bead ς^b is modeled as $\varsigma^b = 3\pi\eta_s\sigma/2\ln(\sigma/a)$, which matches the

averaged translational frictional coefficient of an ellipsoid, of which the radii for the major and minor axes are a and $(1/2)\sigma$, respectively [Berg (1993)]. $\boldsymbol{F}_i^B$ is the Brownian force due to random collision with the surrounding medium molecules, which can be represented as follows [Öttinger (1996)]:

$$< \boldsymbol{F}_i^B(t) >= 0$$

$$< \boldsymbol{F}_i^B(t)\boldsymbol{F}_j^B(t') >= 2k_B T \varsigma^b \delta_{ij}\delta(t-t')\boldsymbol{\delta} \,. \tag{15}$$

$\boldsymbol{F}_i^C$ is the constraint force required to maintain the distance between the two beads constant. The constraint force is the Dirac delta function because the rigid-rod potential is zero unless the rod length is σ. The constraint force is applied with a three-step predictor-corrector algorithm [Somasi *et al.* (2002)]. First, the beads move because of electrophoretic and Brownian force with no constraint force. Then, the tension between the two beads is calculated, and this tension is finally applied to each bead such that the distance between the two beads is constrained as σ.

In this work, Eq. (14) is non-dimensionalized by the following characteristic length, time, and electric field as follows:

$$\hat{r} \equiv r/t_s, \; \hat{t} \equiv t/(\varsigma_c t_s^2/k_B T), \; \hat{E} \equiv E/E_{av}, \; \hat{F} \equiv F/(k_B T/t_s), \tag{16}$$

where ς_c is the characteristic friction coefficient defined as $\pi\eta_s t_s$. The

final non-dimensionalized equation for the bead evolution equation is as follows:

$$d\hat{\boldsymbol{r}}_i^b / d\hat{t} = [Pe^b \hat{\boldsymbol{E}}(\hat{\boldsymbol{r}}_i^b) + 1/\hat{\varsigma}^b (\hat{\boldsymbol{F}}_i^B + \hat{\boldsymbol{F}}_i^C), \qquad (17)$$

where Pe^b is the bead Peclet number defined as $\varsigma_c \mu_0 E_{av} t_s / k_B T$ and $\hat{\varsigma}^b$ is the dimensionless bead friction coefficient $\varsigma^b / \varsigma_c$. $\hat{\boldsymbol{F}}_i^B$ denotes $\sqrt{24/d\hat{t}} \boldsymbol{N}_R$, where $\boldsymbol{N}_R$ is the random number distributed uniformly on the interval [-0.5,0.5] [Grassia *et al.* (1995)].

3.1.2. Calculation of electric field (Finite element method)

The electric potential and electric field are computed by employing FEM. The electric potential V is computed by solving the following Laplace equation:

$$\nabla^2 V = 0 \qquad (18)$$

The essential boundary conditions are imposed on the inlet and outlet as $V_{in} = -\Delta V$ and $V_{out} = 0$. No flux boundary condition ($\partial V / \partial \boldsymbol{n} = 0$, where $\boldsymbol{n}$ is the unit normal vector of the boundary) is imposed on the walls, which means that the walls are assumed to be electrically insulated. The electrical potential is calculated by using the standard Galerkin FEM [Crochet *et al.* (1984)], where V is interpolated with the 9-node biquadratic shape function (P_2^1). The electric field is computed from the relationship $\boldsymbol{E} = -\nabla V$.

3.1.3. Calculation of electrophoretic stream function (Finite element method)

In order to track a molecule following electrophoretic streamlines, the electrophoretic stream function Ψ is calculated by solving the following equations:

$$E_x = \partial\Psi / \partial y, \ E_y = -\partial\Psi / \partial x$$

$$\Psi(\text{upper wall}) = 1, \ \Psi(\text{lower wall}) = 0,$$

(19)

where Ψ is interpolated with the 9-node biquadratic shape function (P_2^1). The line of the iso-electrophoretic stream function constitutes an electrophoretic streamline.

3.1.4. Addressing electric field

The local electric field at the bead position $\boldsymbol{E}(\boldsymbol{r}_i^b)$ is linearly interpolated with the 4-node P_1^0 shape function from the pre-calculated electric fields. For accurate electric field information, more than 100,000 finite element meshes were used. To address the electric field at specific locations, it is necessary to determine the finite element including the bead [Kim *et al*. (2006)]. In order to resolve this issue, Kim and Doyle [Kim *et al*. (2006)] developed an efficient method—"target-induced searching algorithm"—based on graph theory. Although this algorithm is very efficient, we adopted a simpler method to determine an element that includes the bead after the time increment. First, we assessed whether the bead is still included in the element at the previous time step E_0. If it is not, we checked the element E_1 directly adjacent to the element E_0. If the bead does not exist in E_1, we further checked the second neighboring element E_2, which shares nodes with E_1 in succession. If the algorithm fails to find the element that includes the bead up to this step, then all the elements are checked. We adopted $d\hat{t}$ to $10^{-5}/Pe^b$ for $Pe^b > 1$ and 10^{-5} for $Pe^b \leq 1$. Whether the bead is in an element is determined by the algorithm of

point-in-polygon (PIP).

3.2. Simulation parameters

The averaged DNA mobility through the nanofilter arrays is represented by the transit mobility, $\mu = ml_t^2 / \Delta V t_{total}$, which indicates the electrophoretic mobility of the DNA molecules over m unit channels during the total passage time t_{total}. In this work, the transit mobility is normalized with the theoretical maximum mobility for a single point particle in a nanofilter channel with a right angle [Streek et al. (2004)] as follows:

$$\mu_{max} = \frac{\mu_0}{[\alpha + (1-\alpha)\delta][\alpha + (1-\alpha)/\delta]} \qquad (20)$$

In order to investigate the dynamics of DNA molecules in nanofilter arrays, three different sized DNA molecules ($\sigma = 1.67t_s$, $2.83t_s$, and $4.00t_s$) and four different types of tapered channels ($\theta = 45^\circ$, 90°, 120°, and 135°) are considered, respectively. As depicted in Fig. 1.1, the Cartesian coordinates x and y represent the longitudinal and thickness directions, respectively. In the calculations, the effect of the depth direction is neglected. The origin is located at the center of the bottom of the shallow slit. The thickness of the deep well, t_d, is 5 times the shallow channel thickness, i.e., $t_d = 5.00t_s$, and the lengths of the shallow part l_s and total unit channel l_t are $25/3t_s$ and

$75/3t_s$, respectively. The DNA filtration process is calculated over 1000 periodic unit channels ($m=1000$) in order to obtain statistically significant data.

3.3. Results and discussion

3.3.1. High-throughput separation mechanism

The dynamics of three different-sized rod-like molecules ($\sigma = 1.67t_s$,

$2.83t_s$, and $4.00t_s$) were studied in 1000 repeated periodic right-angled

tapered channels, and their corresponding reduced mobilities are shown in

Fig 3.1. We observed that the reduced mobility decreased with increasing rod

size (σ) in a low Pe^b regime, and the reverse was observed in a high Pe^b

regime. The order of mobility at both low and high Pe^b regimes is

consistent with previous works [Fu *et al.* (2005), Laachi *et al.* (2007), *Li et al.*

(2008)]. The mechanisms for the dynamics of rod-like molecules in two

regimes have been explained by Ogston sieving [Fu *et al.* (2006)] and by

torque-assisted separation with a non-uniform electric field [Laachi *et al.*

(2007)], respectively. In addition, the cross-over point (compression of three

bands) is predicted to occur around $Pe^b \sim 0.3$, which is also consistent with

the experimental [Fu *et al.* (2005)] and numerical [Laachi *et al.* (2007)]

results.

In the case of high Pe^b, we postulate that the dynamics of rod-like
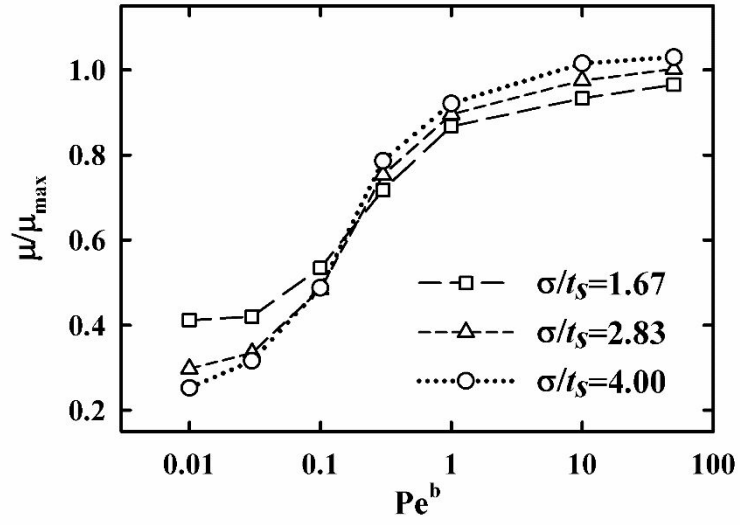
Fig. 3.1. Reduced mobility of the bead-rod molecules in the right angle channel.

molecules is strongly determined by the constraint effect of the molecule after the shallow slit. When the conformation of the rod-like molecule is negative in the shallow slit ($\varphi < 0$), the constraint between the wall and rod affects the position of the fore bead and the conformation of the molecule, as explained in Fig. 2.1. Moreover, the constraint effect is dependent upon the molecular size. Fig. 3.2 schematically shows the rod size-dependent constraint effect and its effect on the lateral displacement. The upper panel of the figure illustrates the motion for the short molecule, while the lower panel shows the motion of the relatively long molecule. From this, it is apparent that the longer molecule moves close to the upper wall due to the constraint effect whereas the short one is less affected by the non-penetrating constraint of the corner.

The size-dependent constraint effect was quantified with a change in the electrophoretic stream function at the fore bead position. We assumed for this model case that the fore bead was initially at the corner of the channel exit, and the aft bead was on the upper wall ($\varphi < 0$). We traced the electrophoretic stream function (Ψ_b^{fore}) at the fore bead position until the aft bead leaves the shallow channel, when the Brownian motion is essentially negligible ($Pe^b = 100$). As defined in Eq. (19), Ψ_b^{fore} was zero at the bottom wall and
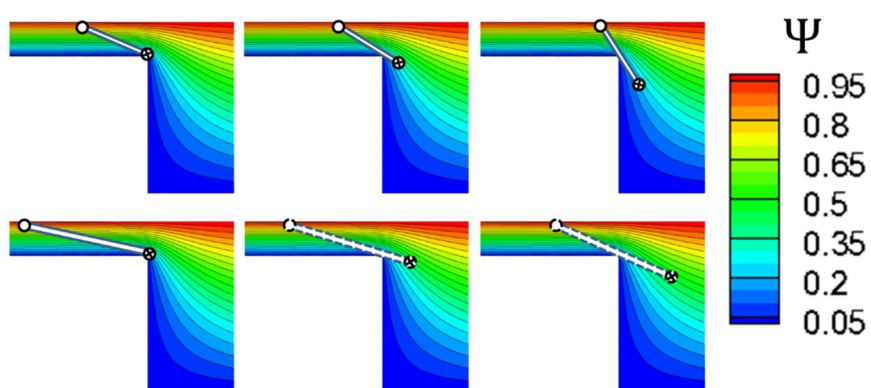
Fig. 3.2. Schematic representation of a molecule leaving the shallow slit when the slope is positive (upper panel) and negative (lower panel).

Ψ_b^{fore} when $\sigma = 1.67t_s$, $2.83t_s$, and $4.00t_s$. As the rod-like molecule the

value was one at the upper wall. Fig. 3.3 shows the temporal change of

escaped the shallow slit, Ψ_b^{fore} changed from 0 to a finite value until the aft

bead had escaped the shallow slit completely. The increment from its initial

(0) to the final values was denoted as $\Delta\Psi_b^{fore}$ (the inset of Fig. 3.3 depicts

$\Delta\Psi_b^{fore}$ with respect to σ). Here, the electrophoretic stream function

gradually changed when the rod-like molecule escaped the shallow slit, and

$\Delta\Psi_b^{fore}$ was significantly dependent upon the rod size, σ (Fig. 3.3). In

contrast, when the rod-like molecule had the conformation of a positive slope

($\varphi > 0$) in the shallow slit, there was little constraint between the rod and

corner wall such that the two beads were able to experience electrophoretic

motion freely [Fig. 2.2 and Fig. 3.4]. In this case, both beads were traced

along the electrophoretic streamline relatively free such that Ψ_b^{fore} was

almost constant during the fore bead translation, and $\Delta\Psi_b^{fore}$ was almost

zero irrespective of σ. In the real process, the probability of the rotational

angle of the rod-like molecule in a shallow slit being negative is one half, but

the constraint effect
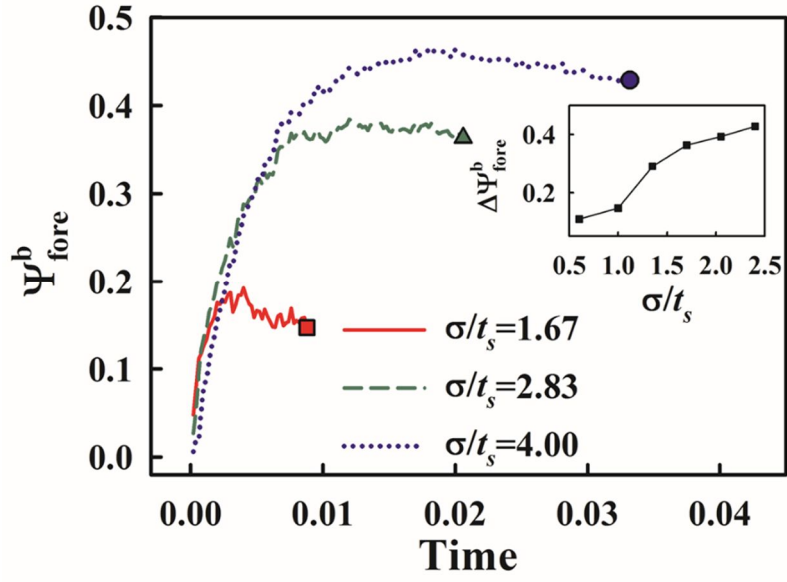
Fig. 3.3. Temporal electrophoretic stream function change as a function of time, and the difference between the initial and final stream functions (inset) when $Pe^b = 100$.
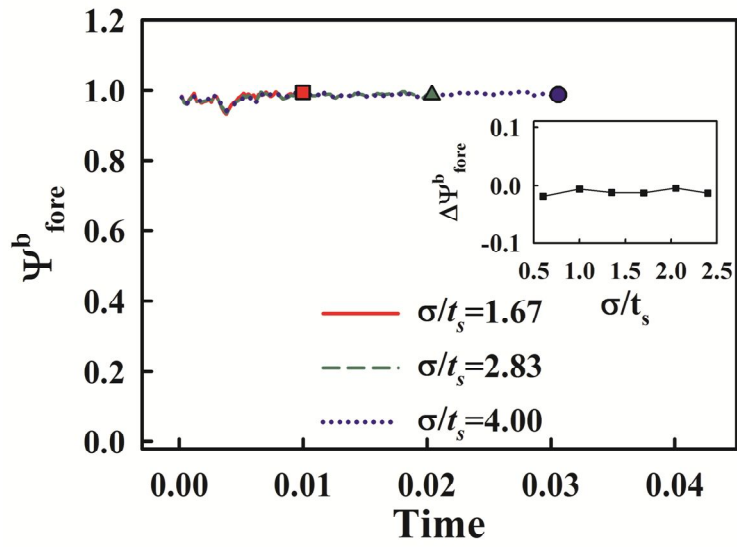
Fig. 3.4. Electric stream function change of forward bead with respect to time and value of the change with respect to rod size.

determines lateral displacement in the whole filtration process. The lateral displacement was observed with the probability distribution of the centroid of the rod-like molecule in the calculation for the entire filtration. Fig. 3.5(a) and 3.5(b) show the distribution of the location of the short ($\sigma = 1.67t_s$) and long ($\sigma = 4.00t_s$) rod-like molecules in the deep well, respectively, when $Pe^b = 10$. As shown in Fig. 3.5(a) and 3.5(b), we divided the deep well into four parts (I: upper entrance, II: upper exit, III: lower exit, IV: lower entrance) and checked the centroid location of the two beads over 1000 periodic filtration channel processes. We found that the long rod-like molecule was located in regions I and II more frequently than in regions III and IV, which was in contrast to the distribution of the short rod-like molecules. This difference in distribution cannot be explained if only the "torque-assisted separation mechanism" is dominant, since the probability in region I is not dominant over other regions.

In order to obtain more detailed information regarding the probability distribution of a rod-like molecule, we also plotted the one-dimensional (1D) probability distributions projected along x- and y- axes (Fig. 3.6(a) and 3.6(b)). The distribution denotes the probability which a molecule exists at specific locations along the axes. The coordinates correspond to the spatial location
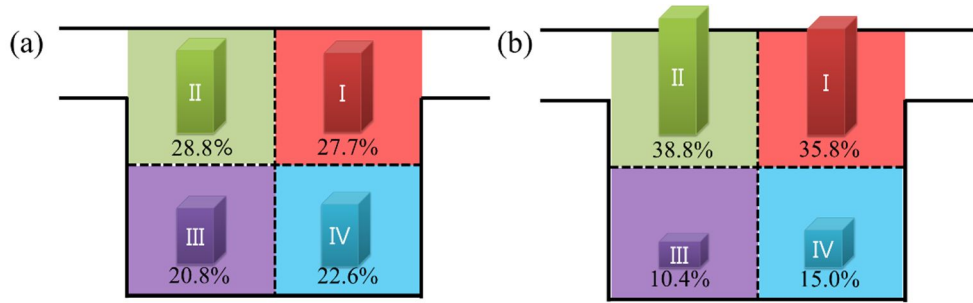
Fig. 3.5. Probability distribution of the center of the molecule in the four regions in the deep well and the inlet and outlet of the shallow slit when (a) $Pe^b = 10$ and $\sigma / t_s = 1.67$ and (b) $Pe^b = 10$ and $\sigma / t_s = 4.00$.
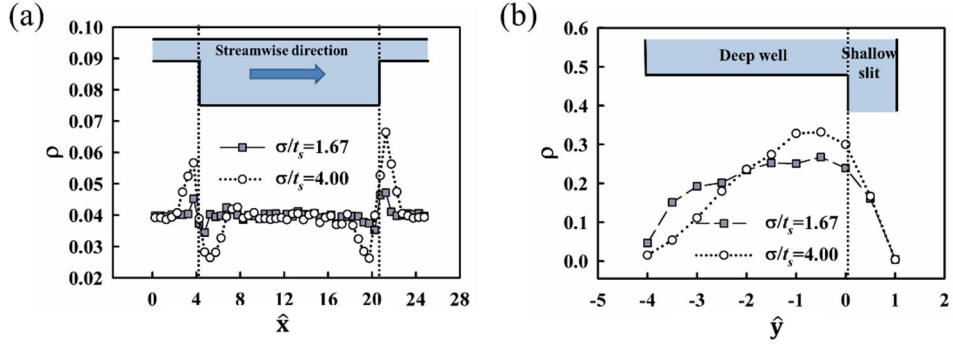
Fig. 3.6. One-dimensional probability distributions of the center of a molecule along (e) $\hat{x}$ - and (f) $\hat{y}$ - axes at $Pe^b = 10$. The coordinates correspond to a specific location of a channel which is denoted by the insets of Fig. 3e and 3f and the coordinates ($\hat{x}$ and $\hat{y}$) were normalized with the thickness of a shallow slit. The arrow in the inset of Fig. 3e denotes streamwise direction.

defined by the insets of Fig. 3.6(a) and 3.6(b) and the coordinates ($\hat{x}$ and $\hat{y}$) were normalized with the thickness of shallow slit. We compared two different sizes of molecules ($\sigma = 1.67t_s$ and $\sigma = 4.00t_s$) at $Pe^b = 10$. The distribution along $\hat{x}$-axis is rather complicated around the entrance and exit of a shallow slit. As compared to the small molecule ($\sigma = 1.67t_s$), the long molecule ($\sigma = 4.00t_s$) has lower probability just before the entrance region ($\hat{x} \sim 20$) of the shallow slit, which corresponds to short dwelling time in the region but the probability sharply increases just after the entrance corner ($\hat{x}$ >20). When we estimated the overall probability around the entrance region ($\Omega_{ent} : 15.75 \leq \hat{x} \leq 22.75$; this region was selected to include the area where the probability distribution significantly changes around the entrance of a shallow slit), there was no significant difference between the two molecules ($\int_{\Omega_{ent}} \rho_{short} d\hat{x} = 0.2998$, $\int_{\Omega_{ent}} \rho_{long} d\hat{x} = 0.3002$). This result is in contrast to the predicted distribution by "torque-assisted separation mechanism" since it is expected that the long molecule has significantly short dwelling time if the "torque-assisted separation mechanism" is dominant. We speculate that the complicated distribution around the entrance region originates from the combined effects of the abrupt change of electric field around the entrance

region and channel constriction. In the exit region of the shallow slit ($\Omega_{\text{exit}} : 1.25 \leq \hat{x} \leq 8.25$), there is also no significant difference in the integrated probability values around the exit region ($\int_{\Omega_{\text{exit}}} \rho_{\text{short}} d\hat{x} = 0.2997$, $\int_{\Omega_{\text{ent}}} \rho_{\text{long}} d\hat{x} = 0.2961$). However, the distribution along $\hat{y}$ -axis clearly demonstrates that the probability distribution of long molecule ($\sigma = 4.00 t_s$) skews toward the upper wall as compared to small molecule case, which is consistent with Fig. 3.5(b) and our previous discussion: the constriction effect at the exit of the shallow slit makes long molecule move closer to the upper wall as compared to small molecule.

In the case of $Pe^b > 10$ and $\sigma > t_s$, the translational diffusion time in the deep well was much longer than that of the electrophoretic motion time in deep well ($\tau_{d,t} / \tau_{e,d} \sim O(10)$). Thus, the lateral position of long rod-like molecules due to the constraint effect changes less by translational diffusion motion as compared to short ones. We emphasize that this difference in lateral distribution does not originate merely from the size-dependent diffusion coefficient and this effect is deterministic.

Thus, we determined that the deterministic constraint effect is responsible for the high-throughput separation mechanism, which implies that the optimal design of the channel shape (affecting the distribution of

electrophoretic streamlines) is essential in enhancing the DNA separation performance.

3.3.2. Effect of the tapered angle on the separation of rod-like molecules

The effect of tapering angle on separation performance for long-chain DNA (10 kbp <M.W.< 100 kbp) has been observed experimentally [Han *et al.* (1999)] and numerically [Duong-Hong *et al.* (2008)] when $\theta \le 90^{o}$ and $E_{av} \sim 100\,\text{V/cm}$. In long chain DNA separation, the separation performance was improved as tapering angle was increased, [Han *et al.* (1999), Duong-Hong *et al.* (2008)] and it is reported that the obstruction of "tumbling along the wall" in tapered channel decreases the separation performance [Duong-Hong *et al.* (2008)].

To investigate the effect of tapering angle on separation performance for short chain DNA, we performed the simulation of the nanofilter process with four differently tapered geometries ($\theta = 45^{o}$, 90°, 120°, and 135°). The thickness of the deep well and length of the shallow slit and the number of total periodic channels were the same as those of the right angle channel ($\theta = 90^{o}$), respectively [$t_d = 5.00t_s$, $l_s = 25/3t_s$, $m = 1000$]. First, the filtration mobility of the three rod-like molecules ($\sigma = 1.67t_s$, $2.83t_s$, and $4.00t_s$) in four channels was investigated with respect to Pe^b. Fig. 3.7

shows the reduced transit mobility, $\mu / \mu_{\max}$, of the three rod-like molecules within the four channels. The trends of $\mu / \mu_{\max}$ as a function of Pe^b were similar in terms of the higher mobility for longer rod-like molecules in high Pe^b and the opposite in low Pe^b. However, the mobility difference between long and short rod-like molecules remarkably increased as the tapering angle θ was increased in the high Pe^b regime ($Pe^b = 10$).

To quantify the mobility difference, the standard deviation of reduced mobility $(\mu / \mu_{\max})_{std.}$ was calculated for the three different-sized rod-like molecules. Fig. 3.8 shows $(\mu / \mu_{\max})_{std.}$ with respect to tapering angle θ. For low Pe^b ($Pe^b = 0.01$), $(\mu / \mu_{\max})_{std.}$ has a similar value, when $\theta = 90^{\circ}$, 120°, and 135°, but not for $\theta = 45^{\circ}$. In addition, for high $Pe^b = 10$, $(\mu / \mu_{\max})_{std.}$ gradually increases with θ. For the high Pe^b regime, we
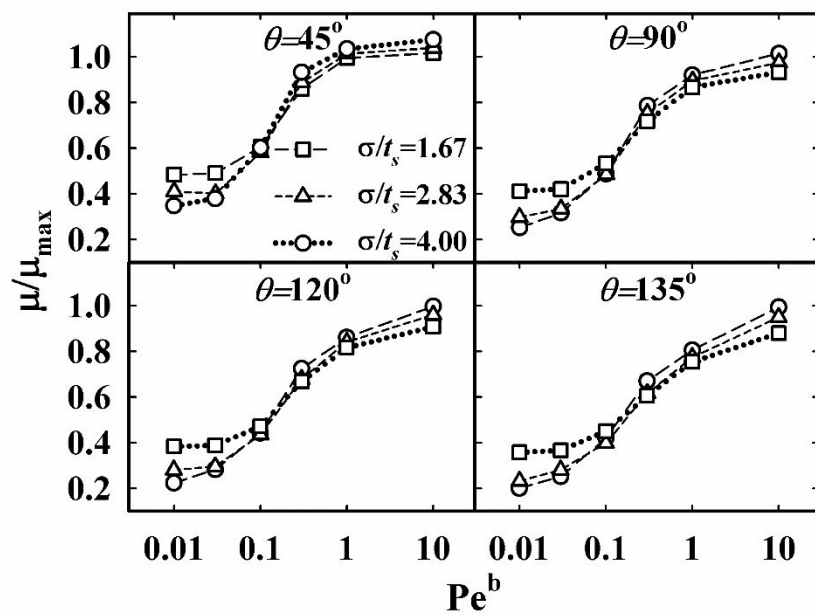
Fig. 3.7. Reduced mobility of the bead–rod molecule in the four tapered channels.
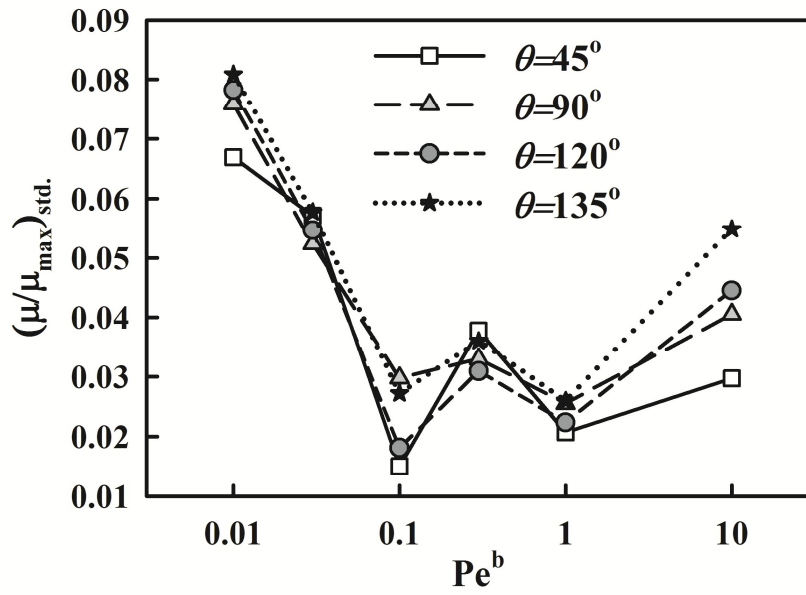
Fig. 3.8. Standard deviations of the reduced mobility.

postulate that the dynamics of rod-like molecules is mostly determined by the constraint effect in a similar way as the right angle channel case. When φ is negative in shallow slit, the constraint effect influences the lateral shift of the rod-like molecule, as the rod-like exits the shallow slit in differently tapered nanofilter channels [Fig. 3.9]. As the molecule leaves the shallow slit, the electrophoretic stream function at the position of fore bead shifts to the higher value compared to the initial value due to the constraint between the rod of the rod-like molecule and the corner wall as in the case of the exiting process in the 90° tapered channel (Fig. 2.1 and Fig. 3.2). However, in the tapered channel, the stream function at the fore bead position is higher in the more tapered channel.

The constraint effect dependent upon molecular size and channel geometry was quantified with a change in the electrophoretic stream function at the fore bead position. We assumed for this model case that the fore bead was initially at the corner of the channel exit, and the aft bead was on the upper wall as the model case of 90° tapered channel. The electrophoretic stream function at the fore bead position was traced from the fore bead exiting the shallow slit to the aft bead exiting the shallow slit completely, and the difference in the stream function values of the fore bead between the initial
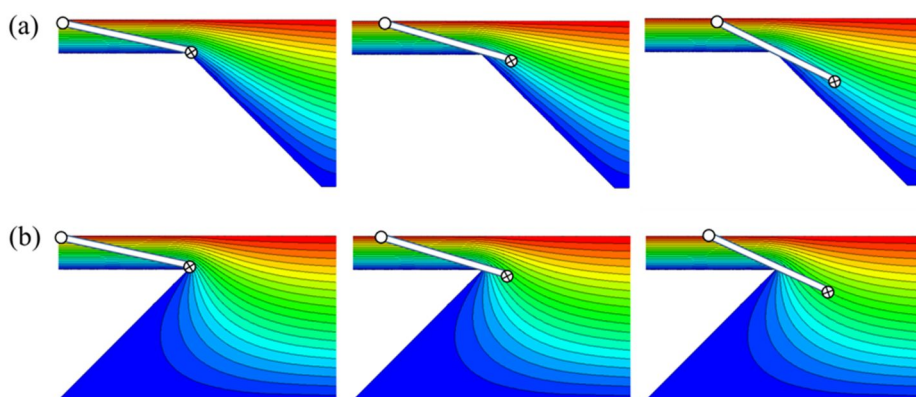
Fig. 3.9. Schematic procedure of constraint effect during molecule exits shallow slit in tapered channel of (a) $\theta = 45^\circ$ and (b) $\theta = 135^\circ$.

and final time step $\Delta\Psi_b^{fore}$ was investigated when the Brownian motion is essentially negligible, ($Pe^b = 100$). Fig. 3.10 shows $\Delta\Psi_b^{fore}$ of three rod-like molecules ($\sigma = 1.67t_s$, $2.83t_s$, and $4.00t_s$) with four differently tapered channels ($\theta = 45^o$, 90°, 120°, and 135°) in the model case simulation. $\Delta\Psi_b^{fore}$ increased as either θ and/or σ increased, which indicates that the constraint effect becomes more significant and can be attributed to the electrophoretic streamline shift of a molecule.

The constraint effect dependent upon molecular size and channel geometry was also observed in the simulation of whole filtration process for the high-throughput regime by averaged electrophoretic stream function, Ψ_{avg}. Over the 1000 periodic filtration process, Ψ_{avg} was averaged from the values of electrophoretic stream function at the position of two beads at every discrete time step. Fig. 3.11 shows Ψ_{avg} of three rod-like molecules ($\sigma = 1.67t_s$, $2.83t_s$, and $4.00t_s$) in four different tapered channels ($\theta = 45^o$, 90°, 120°, and 135°) over 1000 periodic filtration process for $Pe^b = 10$. As
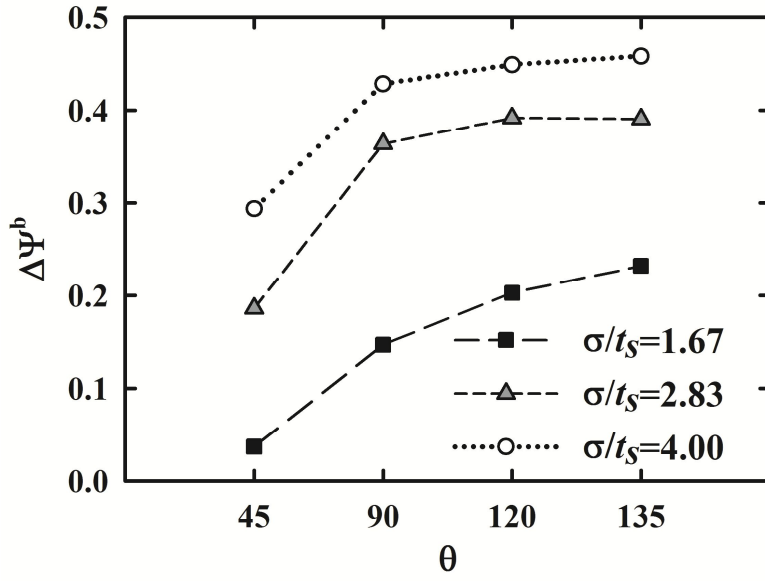
Fig. 3.10. Stream function change of the model in the tapered channel when $Pe^b = 100$.
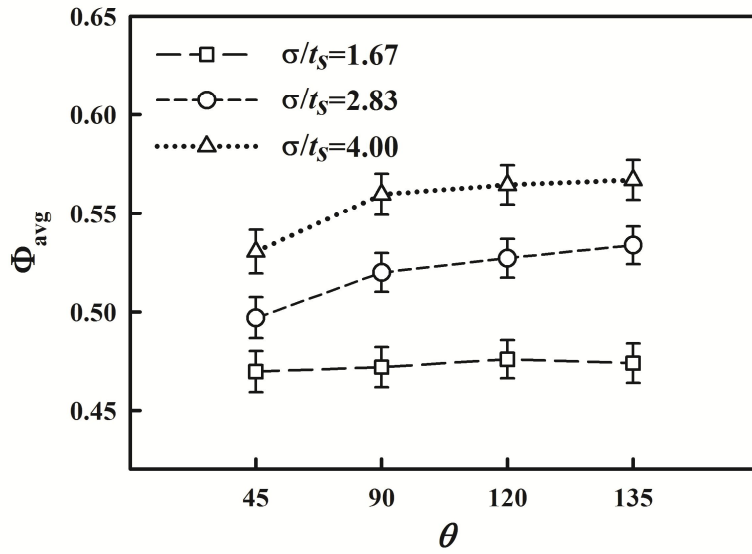
Fig. 3.11. Average stream function at the center position of the molecule over 1000 unit nanofilter processes when $Pe^b = 10$.

shown in Fig. 3.11, Ψ_{avg} of longer molecules is larger than that of shorter

molecules. This tendency is similar to that of the size-dependent shift of the electrophoretic streamline [Fig. 3.2 and Fig. 3.3] and lateral distribution [Fig. 3.5] in the 90° tapered channel; this can be explained by the deterministic separation mechanism of the high-throughput regime. However, in the tapered channel, Ψ_{avg} of the long rod-like molecules ($\sigma = 2.83t_s$ and $4.00t_s$) increases with increasing θ, whereas that of the shortest molecule ($\sigma = 1.67t_s$) does not change significantly. Thus, the difference of Ψ_{avg} between a short ($\sigma = 1.67t_s$) and long molecule ($\sigma = 4.00t_s$) increases with θ. These results indicate that the dependence of molecular size on the electrophoretic streamline along which the molecule translates grows as the tapering angle increases. In the high-throughput regime, the translational diffusion is not relevant and the rotational motion is constricted by the upper wall. In this case, the transition by electrophoretic motion governs the transit mobility in the whole filtration process. Therefore, the more highly tapered channel brings stronger dependence of molecular size on the transit mobility and better performance of the separation process.

The lateral displacement by constraint effect according to channel geometry was also investigated through the distribution of probability for rod-like molecule location [Fig. 3.12]. For $\theta = 45^\circ$, the distribution of

probability for rod-like molecules is similar for both short ($\sigma = 1.67t_s$) and long ($\sigma = 4.00t_s$) molecules. However, for $\theta = 135^\circ$, the distribution of the long molecules becomes more heterogeneous than that of short molecules. Thus, the constraint effect involved lateral displacement of molecules in the deep well, and the degree of the lateral displacement can be related with the tapering angle of the channel, at the high-throughput regime.

   With this information, the deterministic separation mechanism in high-throughput regime becomes more distinct as the tapering angle increases. We expect that the mechanism proposed in the current work can be applied in designing more efficient nanofilter channels.
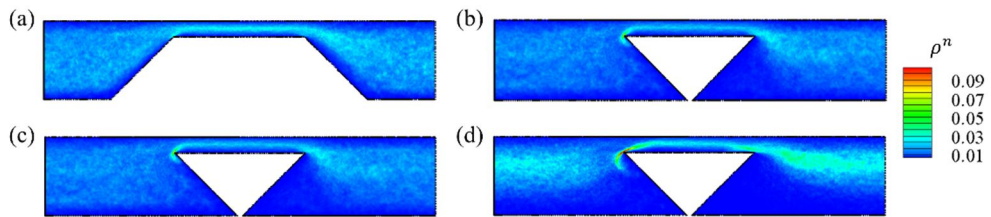
Fig. 3.12. Probability distribution of center of molecule when (a) $\theta = 45^\circ$, $\sigma = 1.67 t_s$, (b) $\theta = 45^\circ$, $\sigma = 4.00 t_s$, (c) $\theta = 135^\circ$, $\sigma = 1.67 t_s$ and (d) $\theta = 135^\circ$, $\sigma = 4.00 t_s$.

Chapter 4. Aggregating particle under 4:1 planar contraction channel flow

4.1. Numerical methods

4.1.1. Boundary conditions

The particle which deviates the channel domain was enforced to reflect normal to the wall. The boundary condition of u_z at inlet and outlet surface was obtained from the analytic solution of Newtonian creeping flow in duct channel assuming that the flow was fully developed and uni-directional. If the pressure difference on inlet plane is $(dp/dz)_{in}$, the boundary condition of inlet flow velocity $u_{z,in}$ could be derived as Eq. (21), where the Peclet number Pe is the dimensionless shear rate defined in Eq. (22).

$$u_{z,in} = Pe \frac{L_{x,up}}{2A} \sum_{n,m=1}^{\infty} \frac{\left((-1)^n - 1\right)\left((-1)^m - 1\right)}{nm\left(\beta^2 n^2 + m^2\right)} \sin\left(\frac{n\pi\left(x + 0.5L_{x,up}\right)}{L_{x,up}}\right) \sin\left(\frac{m\pi\left(y + 0.5L_{y,up}\right)}{\beta L_{x,up}}\right)$$

$$A = \sum_{k,l=1}^{\infty} \frac{4(-1)^{k+l}}{(2k-1)(2l-1)\left(\beta^2 (2k-1)^2 + (2l-1)^2\right)}, \qquad (21)$$

$$\beta = L_{y,up} / L_{x,up}$$

$$Pe = \frac{6\pi\eta a^3}{k_B T} \dot{\gamma}_{avg} = \frac{6\pi\eta a^3}{k_B T} \frac{8A\beta^2 L_{x,up}^2}{\eta\pi^4 L_{x,up}} \left(\frac{dp}{dz}\right)_{in} \qquad (22)$$

4.1.2. Addressing velocity field

To address $u_i^m(r_i)$ at the position of the particle i, it is necessary to find out the finite element that includes the particle. We used a method of 'searching in neighboring elements' to find out an element that includes the particle after time increment whose detail processor is explained in Section 3.1.4. The criterion whether the particle is in an element is described follows.

First, two opposite diagonal nodes in the hexahedron element are selected arbitrarily as reference nodes. And then, three basis vectors toward neighboring nodes are determined on each reference nodes. If the position of particle is expressed as positive linear combination of basis vectors from both reference nodes, the particle is inside of the element.

If an element that includes the particle is determined, the velocity at that particle position is assigned as interpolated from the nodal velocities of the element obtained at previous time step.

4.1.3. Injection of particle

At every time interval Δt, n ($n = 3\phi_{in} Q \Delta t / 4\pi a^3$) particles were injected into the channel which was filled with fluid with no particle in the beginning. ϕ_{in} is the volume fraction of the particle at inlet ($\phi_{in} = 0.1$) and Q is the volumetric flow rate. The particle distribution at the inlet surface

was set proportional to the velocity profile. If the particle distribution on inlet plane is not proportional to the velocity profile, local volume fraction of particle not homogeneous. If the particle is injected on inlet surfaces uniformly at each time step, for example, more particles with large clusters exist close to the wall and it is unrealistic.

4.2. Simulation domain and parameters

The simulation domain is shown in Fig. 4.2. The Cartesian coordinates x, y, z represent contraction, vorticity and main flow direction, respectively. The y-directional depth L_y is $62.5a$ and the width of upstream $L_{x,up}$ and downstream $L_{x,down}$ is $100a$ and $25a$ respectively, so that the channel has a planar 4:1 contraction shape. Calculation of the two

parts (BD and FEM) was conducted alternatively and repeatedly sharing $\boldsymbol{u}_i^m$

and $\boldsymbol{\tau}_p$.

The interparticle potential used in this study was the Lennard-Jones potential,

$$U(r_{ij}) = 4U_w[(2a/r_{ij})^{12} - (2a/r_{ij})^6],\qquad(23)$$

where U_w is the well depth of the potential, a is the radius of the particle and r_{ij} is the distance between the particle i and j. The Lennard-Jones potential was used here to simply represent the balance between the attractive ($r_{ij} > 2\sqrt[6]{2}a$) and repulsive forces ($r_{ij} < 2\sqrt[6]{2}a$) as the potential curve in Fig. 4.1 shows. In this study, we modeled 4:1 planar contraction flow of aggregating particle suspensions with the condition of $Pe = 10$,
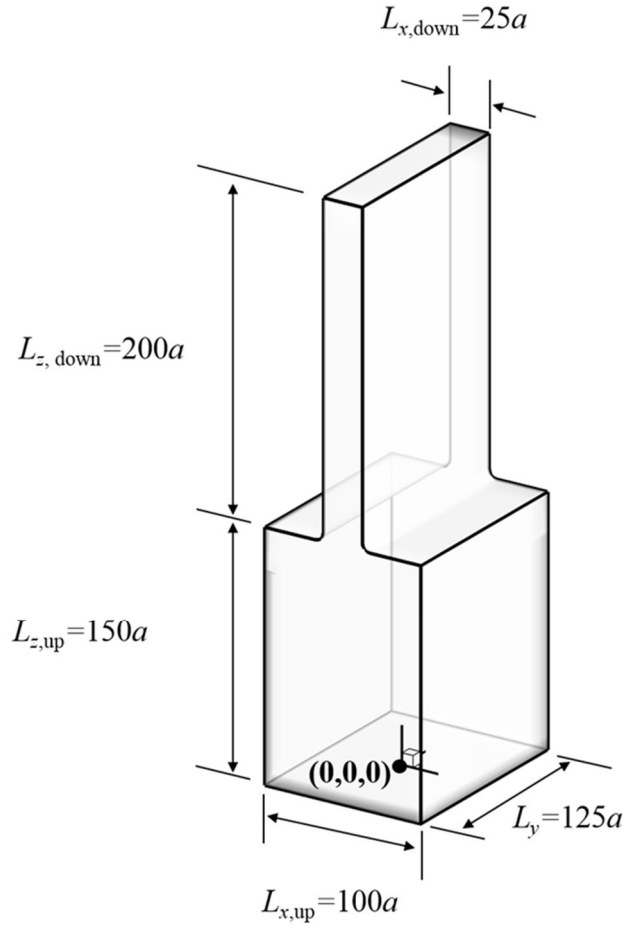
Fig. 4.1. Schematic design of 4:1 micro-contraction channel. $L_{z,up}$ and $L_{z,down}$ are the channel length of upstream and downstream to flow direction, $L_{x,up}$ and $L_{x,down}$ are the width of upstream and downstream to contraction direction, and L_y is the length in depth direction. Origin is located at the center of inlet plane.

$U_w / k_B T = 10$ unless mentioned otherwise. The vortex re-attachment length

was in the range of 13 ± 1.7 such that the length of upstream ($L_{z,up} = 150$)

was long enough to ignore the effect of entrance on vortex dynamics.

In this simulation, length, time, and force were non-dimensionalized

by the characteristic values of a, $\varsigma a^2 / k_B T$ and $k_B T / a$ respectively such

that Eq. (4) is non-dimensionalized and discretized as

$$\Delta \tilde{\boldsymbol{r}}_i = [\tilde{\boldsymbol{u}}_i^m (\tilde{\boldsymbol{r}}_i) + \tilde{\boldsymbol{F}}_i^P + \tilde{\boldsymbol{F}}_i^B] \Delta \tilde{t}. \tag{24}$$

$\tilde{\boldsymbol{F}}_i^B$ denotes $\sqrt{24 / \Delta \tilde{t}} N_R$, where N_R is the random number distributed

uniformly on interval [-0.5,0.5] [Grassia *et al.* (1995)]. The difference

equation (Eq. (24)) is solved by the time marching scheme of Euler method.

The total number of finite element was 8,316 and the degree of freedom was

about 230,000. When the particles were fully filled in the channel, the total

number of particles was about 80,000. The time step was 5×10^{-5}. According

to previous report about verification of SC algorithm [Myung *et al.* (2011)],

the relative viscosity converged when the time step was lower than 1×10^{-3} at

$Pe = 1$. As Pe is larger in this simulation ($Pe = 10$ at inlet), we set the time

step as 5×10^{-5}. In the results, the variables are expressed as dimensionless

unless mentioned otherwise and the superscript '~' is dropped for

convenience.
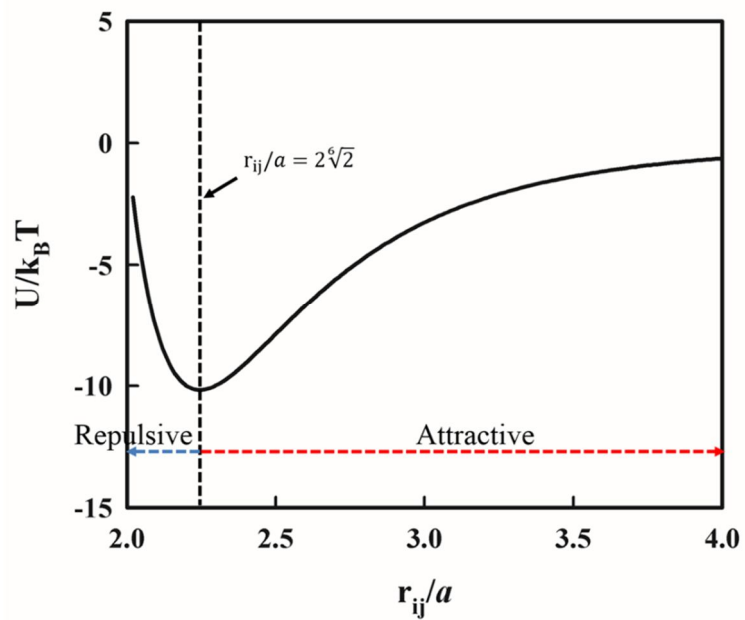
Fig. 4.2. Lennard-Jones potential curve

4.3. Results and discussion

4.3.1. Heterogeneity in particle clustering

The aggregating particles formed particle structures as they flow in the contraction channel. Fig. 4.3 shows one of cluster formation and extinction on the center plane (y=0). The color of particle indicates cluster size of ith particle belonging $N_{cl}(i)$, where the cluster size is the number of particle in the cluster. As Fig. 4.3 shows, particles flowing in upstream gathered and formed a small cluster (blue cluster in red circle at t=4.57) and the cluster size increased (green cluster in red circle at t=4.58) by gathering neighbor particles. Sometimes there was merging between clusters (yellow cluster in red circle and skyblue cluster in black circle at t=4.65). And then, large cluster approached contraction entry (red cluster in read circle at t=4.67) and it broke-up by smaller clusters passing contraction entry (two skyblue clusters in red circle at t=4.71). As the snapshots shows, in contraction channel, particle cluster changed according to time and position. First, to get an idea on the particle clusters formed at each channel position more quantitatively, we calculated the element-wise cluster size

$$< N_{cl}^E >= \frac{1}{m} \sum_{i=1}^{m} N_{cl}^E(i)$$ at each finite element E, where m is the number of

particles and $N_{cl}^{E}(i)$ is the number of
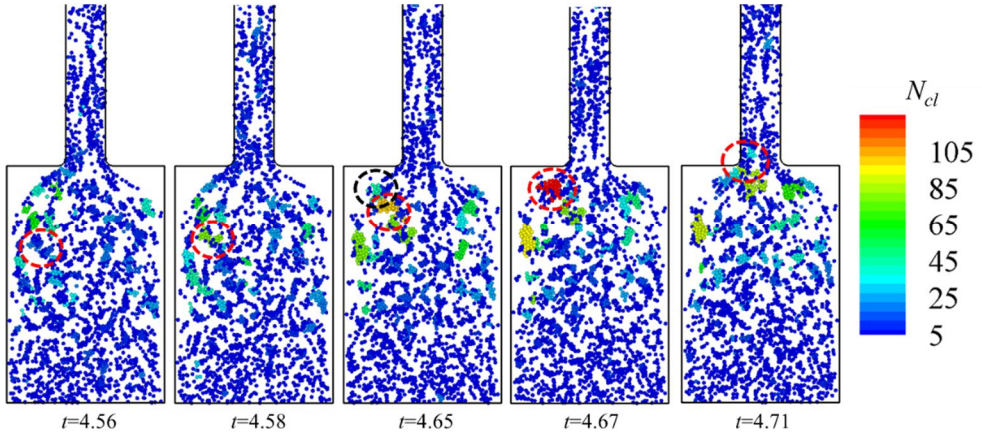
Fig. 4.3. Snapshot of cluster formation and extinction on the center plane (y=0)

particle of the cluster to which the ith particle belongs inside the finite element E. The representation definition of $N_{cl}^{E}(i)$ is schematically illustrated in Fig. 4.4. The nodal average cluster size was defined as

$$N_{cl}^{n} = \frac{\sum V^{E'} \langle N_{cl} \rangle^{E'}}{\sum V^{E'}}$$ for sharing nodes with adjacent element E', where

$V^{E'}$ is the volume of the element E'. We defined the cluster such that a pair of particles belong to the same cluster if the distance between the ith and j[th] particle is shorter than $r_{ij} = 2.26$, where the Lennard-Jones potential corresponds to 98% of the potential well ($U_{r_{ij}=2.26} \approx -0.98 U_{w}$). Fig. 4.5(a) shows the profile of time averaged cluster size $< N_{cl}^{n} >_{st}$ on the center plane (y=0) of the channel. N_{cl}^{n} was averaged for 5<t<20 where the flow was steady for $Pe = 10$ and $U_{w}/k_{B}T = 10$. As Fig. 4.5(a) shows, the particle clusters was formed non-uniformly depending on the position of the channel. The maximum cluster size was observed at around the coordinates (x,z)=(-33.2, 112.4) and (34.2, 112.4), and was about 60.

Fig. 4.5(b) shows $< N_{cl}^{n} >_{st}$ along the streak line of A and B in Fig. 3(a) with respect to z-position, where line A indicates the streak line passing

the origin and B represents the streak line passing the position of maximum

cluster size $(x,z)=(-33.2, 112.4)$. The streak lines were obtained from time

Element E

$$N_{cl}^E(1) = 1$$

$$N_{cl}^E(4 \sim 9) = 6$$

$$N_{cl}^E(2 \text{ and } 3) = 2$$

$$<N_{cl}^E> = \frac{1 \times 1 + 2 \times 2 + 6 \times 6}{9} = 4.56$$
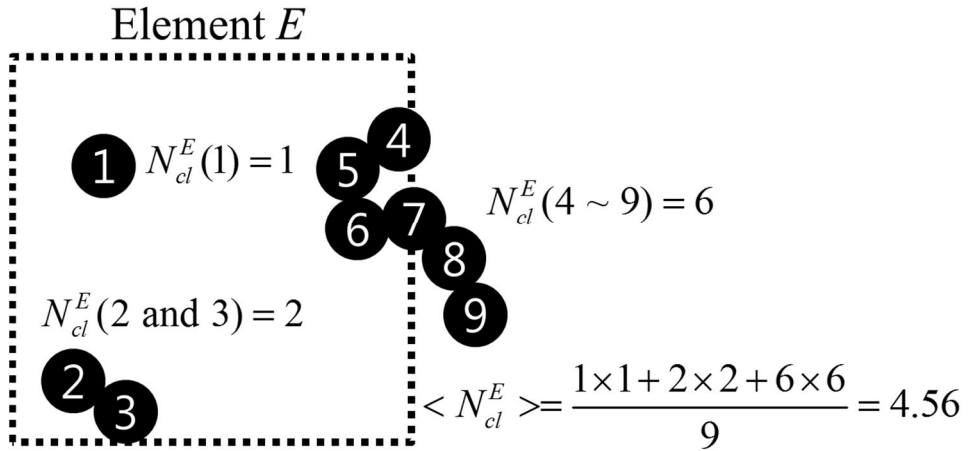
Fig. 4.4. Schematic representation of calculating $<N_{cl}^E>$
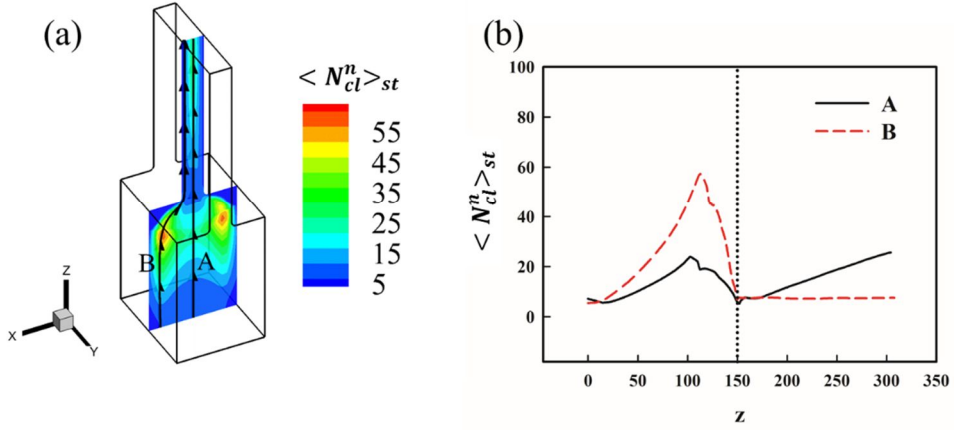
Fig. 4.5. (a) $<N_{cl}^n>_{st}$ on the center plane ($y=0$) at $Pe = 10$ and $U_w/k_B T = 10$. Line A indicates the streak line passing the origin and B presents the streak line passing the position of maximum cluster size (-33.2, 112.4); (b) $<N_{cl}^n>_{st}$ with respect to z-position along the line A(black solid) and line B(red dotted line).

averaged velocity profile for 5<t<20. As Fig. 4.5(b) shows in upstream region (0<z<150), $<N_{cl}^{n}>_{st}$ increased with z-position for 0<z<102.7 in line A and for 0<z<112.4 in line B. After the position where the maximum $<N_{cl}^{n}>_{st}$ was observed, $<N_{cl}^{n}>_{st}$ decreased until contraction entry where a vertical dotted line is indicated (z=150). In upstream region, $<N_{cl}^{n}>_{st}$ in line B was larger than that in line A. In downstream region (150<z<350), $<N_{cl}^{n}>_{st}$ increased with z in line A but it maintained a small value less than 10.

The position dependent formation and breakup of particle clusters arises from the competition of flow and interparticle forces. The flow strength was represented by a second invariant of the rate of deformation tensor II_{D}, where $D = \frac{1}{2}\left(\nabla u + \nabla u^{T}\right)$. The strength of the interparticle force was quantified as a nodal interparticle force $F^{p,n}$. $F^{p,n}$ was volume averaged as $F^{p,n} = \dfrac{\sum V^{E'} F^{p,E'}}{\sum V^{E'}}$ for sharing nodes with adjacent element E', where $F^{p,E'}$ is the average value of the interparticle force in element E'. Usually, the distance between particle pair is larger than the position of

potential well depth in Lennard-Jones potential ($r_{ij} = 2\sqrt[6]{2}a$) when $\phi \sim 0.1$ such that $F^{p,n}$ is negative over the contraction channel. The negative $F^{p,n}$ indicates that the attractive force is applied. N_{cl}^n, II_D and $F^{p,n}$ were averaged for 5<t<20 and Fig. 4.6(a) and (b) show the change of time averaged values of $<N_{cl}^n>_{st}$, $<II_D>_{st}$ and $<-F^{P,n}>_{st}$ with respect to z along the line A and B respectively. The values were normalized by the maximum value of each. The maximum value of $<-F^{P,n}>_{st}$ was about 2,500 in line A and B and that of $<II_D>_{st}$ was about 80 in line A and 200 in line B. As shown in Fig. 4.6(a) and (b), the interparticle force was constant over the whole region except around the contraction entry region (110<z<160). Around the contraction entry region, $<-F^{P,n}>_{st}$ decreased slightly and increased again as z increased. However, the change of $<II_D>_{st}$ showed different shape in line A and line B. In line A, $<II_D>_{st}$ increased steeply to contraction entry and was about 40 in downstream such that the size of cluster increased again in downstream due to the attractive interparticle forces. On the other hand, in line B, $<II_D>_{st}$ increased steeply to contraction entry but was maintained as large as 200 in downstream. Thus the size of cluster maintained small in downstream in line B. Conclusively, the clustering was determined by the competition of flow

and interparticle forces, and different flow characteristics due to geometric

effect influenced heterogeneous formation of clusters.
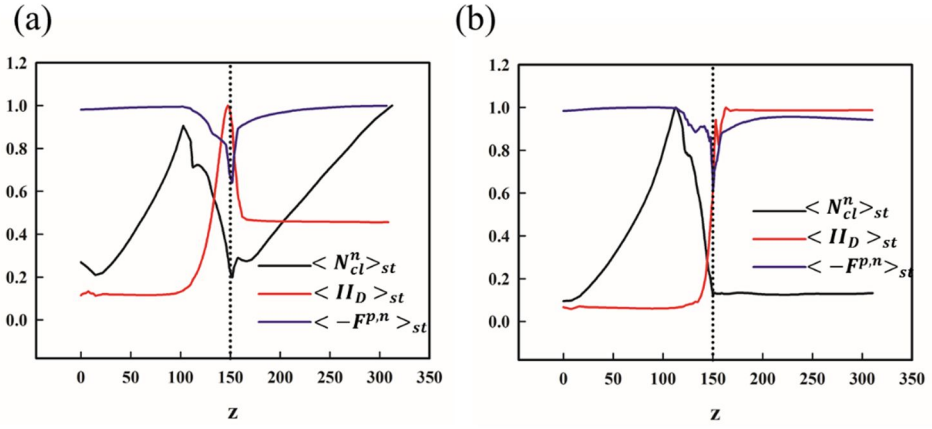
Fig. 4.6. Normalized $<N_{cl}^n>_{st}$, $<II_D>_{st}$ and $<-F^{P,n}>_{st}$ with respect to z-position (a) along the line A and (b) line B, where black dotted line indicates the position of contraction entry (z=150).

4.3.2. Spatio-temporal fluctuation

Another characteristics of the particulate flow in the contraction channel was fluctuation of the flow with respect to space and time, which was not observed in Newtonian fluid without particles. To analyze the fluctuation of the flow characteristics, the degree of fluctuation of the velocity field (u) was defined as the standard deviation ($\sigma(u)$) in the time series for $5 < t < 20$. Fig. 4.7(a), (c) and (e) show $\sigma(u_x)$, $\sigma(u_y)$ and $\sigma(u_z)$ on the center plane ($y=0$) of the channel. They showed maximum values near the contraction entry, and strong fluctuation was observed in the sequence of $\sigma(u_x)$, $\sigma(u_z)$, $\sigma(u_y)$. It is also evidenced in Fig. 4.7(b), (d) and (f), which represent the average velocity $<u_x>$, $<u_y>$ and $<u_z>$ in the contraction entry region which was defined as the dotted box region ($|x| < 12.5$, $|y| < 10$, $134 < z < 142$) in Fig 4.7(a). The amplitude of fluctuation in the velocity field decreased in the sequence of $<u_x>$, $<u_z>$, $<u_y>$ and the standard deviation decreased in the same order as above ($\sigma(<u_x>) = 6.86$, $\sigma(<u_y>) = 2.66$, $\sigma(<u_z>) = 3.95$). The standard

deviation of the velocity field was 1.37%, 0.53%, and 0.79% of the maximum
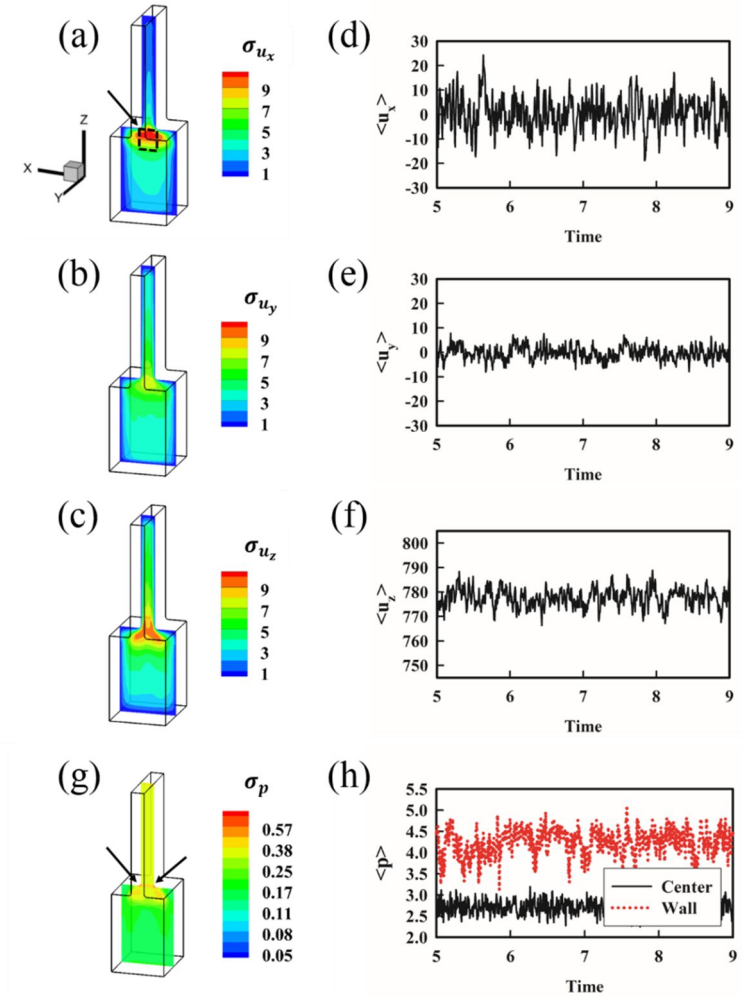
Fig. 4.7. Standard deviations of (a) u_x, (b) u_y, (c) u_z on the center plane (y=0) and the fluctuation in average velocities of (d) u_x, (e) u_y (f) u_z in boxed area $(12.5 < |x| < 17.5, |y| < 10, 150 < z < 155)$; (g) standard deviation of pressure on the center plane (y=0); (h) average pressure in the region close

to the wall $12.5 < |x| < 17.5, |y| < 10, 150 < z < 155$ (red dotted line) and at the center of contraction entry region $|x| < 12.5, |y| < 10, 134 < z < 142$ (black solid line).

velocity at inlet $u_{z,in_{max}} = 0.5 Pe L_x = 500$. It is to be noted that the variation in contraction (x) direction was larger than the variation in flow (z) direction. This implies that the effect of particles was highly anisotropic in the contraction flow. As shown in Fig. 4.7(g), the position dependent pressure fluctuation (σ_p) was largest in the corner of the contraction entry (see black arrow). Fig. 4.7(h) shows the average pressure $<p>$ near the wall (red dotted line; $12.5 < |x| < 17.5, |y| < 10, 150 < z < 155$) and at the center of the contraction entry region (black solid line; $|x| < 12.5, |y| < 10, 134 < z < 142$). The amplitude of fluctuation at the wall of contraction entry (red dotted line) was larger than that at the center (black solid line). This provides a useful information in designing the microchip and in analyzing the pressure profile which strongly depends on the position of the pressure sensor in microchannel experiments.

The fluctuation was related with the formation and breakup of particle structures. Fig. 4.8(a) shows the average cluster size $\overline{N}_{cl}$ as a function of time in the contraction entry region (-12.5<x<12.5, 125<z<150).

The particles were injected into the channel and reached the contraction entry region at $t \approx 0.28$, after which $\overline{N}_{cl}$ changed between 100 and 500. The degree of clustering was dependent on the strength of the interparticle potential force,
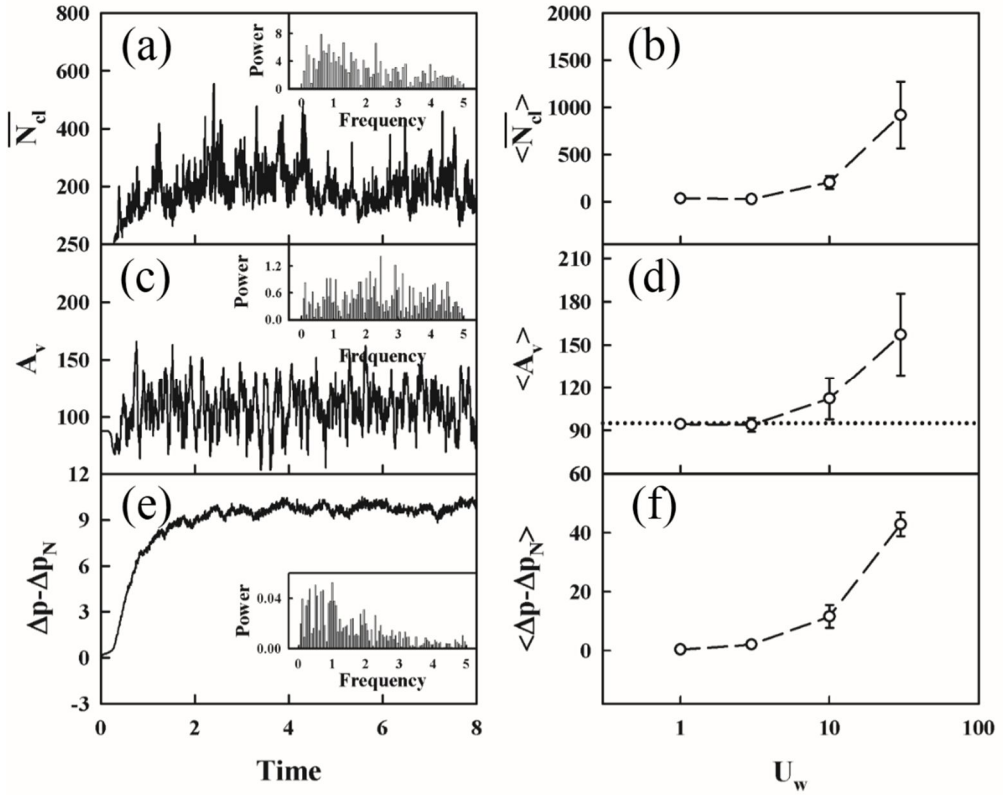
Fig. 4.8. Temporal fluctuations of (a) cluster size in the region of contraction entry (-12.5a<x<12.5a, 125a<z<150a), (b) time average cluster size in the region of contraction entry (-12.5a<x<12.5a, 125a<z<150a), (c) vortex size in $x > 0$, (d) vortex size in $x > 0$, (e) difference in pressure drop between inlet and outlet surface and that of Newtonian fluid, and (f) difference in

pressure drop with respect to U_w. The inlets in (a), (c) and (e) are the power spectrum of Fourier Transformed time series.

which was represented by U_w. Fig. 4.8(b) shows the time averaged cluster size $<\bar{N}_{cl}>$ and its standard deviation (see error bar in the figure.) in the contraction entry region (-12.5<x<12.5, 125<z<150) at U_w/k_BT=1, 3, 10 and 30 for 5<t<20 where the flow was steady. While the particle clustering was rarely observed for U_w/k_BT=1 and 3, the average cluster size $<\bar{N}_{cl}>$ and its standard deviation increased with the increase in U_w, U_w/k_BT=10 and 30 in particular. For U_w/k_BT=1 and 3, the error bar was smaller than the size of the symbol. In other words, the effect of particle structure on the contraction flow becomes significant for $U_w/k_BT \geq 10$.

Fig 5(c) shows the variation of the vortex size at the right hand side of the channel (x>0) at Pe=10 and U_w/k_BT=10. In this study, we defined the vortex size as follows. In the contraction flow, the streak line of rotating vortex exists in the region of contraction entry (100<z<150), where the re-attachment lengh of the vortex shows maximum near y=0 plane. To

characterize the vortex size in three dimension, we checked the re-attached position in x, z coordinates (x_v,z_v) which corresponds to the maximun re-attachment length in thickness direction. The vortex size was assumed to be the area of the right-angled triangle, A_v, which consists of (x_v,150), (50,z_v) and contraction corner(50,150) for the vortex at right hand side. The vortex size on the left hand side was defined in the same way. We defined the re-attachment position x_v,z_v as the point u_x=0, u_z=0, where the velocity becomes opposite to the flow of main stream in the contraction entry region (100<z<150). Symmetric vortices were observed for Newtonian flow with the re-attachment points at ($\pm$33.3,150) and ($\pm$50,139.5), and the vortex size was approximately 95. As shown in Fig 5(c), the vortex fluctuated with time after t=0.28 when the particle cluster first approaches the contraction entry. The time averaged re-attachment points were (-32.8,150) and (-50,137.4) for x<0 and (32.8,150) and (50,137.5) for x>0, and the average vortex size was 112.2 with the standard deviation of 13.7. Here, the size of the vortex was larger than that of the Newtonian fluid by 17.2. Fig. 4.8(d) shows the time averaged vortex size and its standard deviation (see error bar) for $U_w / k_B T = 1,\ 3,\ 10$ and 30. While the vortex size for $U_w / k_B T = 1$ and 3 was not much different from that of the Newtonian flow, the vortex size

for $U_w/k_BT=10$ and 30 showed an increase in 18% and 65%, and the standard deviations (see error bar) were 13% and 19% of the average vortex size, repectively. This means that the change in vortex size depends on the degree of particle aggregation in the contraction flow and the dependency of vortex size on aggregating force (U_w) was similar to that bewteen the average cluster size ($<\bar{N}_{cl}>$) and aggregating force as shown in Fig. 4.8(b).

Fig. 4.8(e) shows the temporal fluctuation of $\Delta p - \Delta p_N$, where Δp is the pressure drop of the suspension and Δp_N is the pressure drop of the Newtonian fluid between inlet and outlet planes in contraction channel. The pressure drop first increased as the channel was filled with particles, and reached steady state. It also showed fluctuation as in the cluster size and vortex size, but the variation was smaller than that of the vortex size. The pressure drop was closely related with the interparticle force as much as the cluster size and vortex size. Fig. 4.8(f) shows the time averaged pressure drop $<\Delta p - \Delta p_N>$ and its standard deviation for $U_w/k_BT=1,\ 3,\ 10$ and 30. Similar to the cluster size and vortex size, the pressure drop showed no signicant difference for $U_w/k_BT=1$ and 3, but it increased significantly as U_w increased to $U_w/k_BT=10$ and 30. In addition, the standard

deviation (error bar) corresponded to 20% of the average pressure drop for

$U_w / k_B T = 10$ and 30. Conclusively, the contraction flow of the

aggregating suspension showed temporal fluctuation in velocity field, vortex

size and pressure drop. And the last two were closely related with the change

in particle clustering. A distinguishing characteristic of this time series of

cluster size, vortex size and pressure drop was complex periodicity with

observable peaks in a wide range of frequencies in Fourier transform

analysis as shown in the inlets of Fig. 4.8(a),(c) and (e).

4.3.3. Correlation of fluctuations

In order to analyze the temporal fluctuation in terms of particle structure, the Pearson's correlation coefficient was calculated, which provides an information on the relationship between the fluctuation of particle cluster size and flow characteristics. Pearson's correlation coefficient ($\rho(X,Y)$) is an index which represents the linear correlation between two variables X and Y. If X and Y shows positive linear correlation, $\rho(X,Y)$ is close to unity; on the other hand, if they show negative linear correlation, $\rho(X,Y)$ approaches minus one. $\rho(X,Y)$ approaches zero as the correlation between X and Y becomes weak. $\rho(X,Y)$ is defined in Eq. (25), where n indicates the number of data points, X_i, Y_i are the couple of ith data, $\overline{X}$, $\overline{Y}$ are the average values, and σ_X, σ_Y are the standard deviations, respectively.

$$\rho\left(X,Y\right)=\frac{1}{n-1}\sum_{i=1}^{n}\frac{\left[\left(X_i-\bar{X}\right)\left(Y_i-\bar{Y}\right)\right]}{\sigma_X\sigma_Y} \qquad (25)$$

We calculated the Pearson's correlation coefficient by plugging particle cluster size in X and vortex size in Y to investigate the correlation between the fluctuations in particle cluster and vortex size. Fig. 4.9(a) and (b) show the Pearson's correlation coefficient $\rho\left(N_{cl}^n,A_v\right)$ at the center plane (y=0) in depth direction, where the cluster size (N_{cl}^n) was chosen to be the X data and the vortex size (A_v) of the left ($x<0$) and right hand side ($x>0$) was chosen as the Y data, respectively. In Fig. 4.9(a) and (b), strong positive correlation was observed around the coordinates (x,z)=(-24.4, 133.9) and (24.6, 134.1) in red region. Even though $\rho\left(N_{cl}^n,A_v\right)$ of left (Fig. 4.9(a)) and right (Fig. 4.9(b)) side were not perfectly symmetric, the fluctuation of the vortex size showed a positive correlation with the particle clusters which locate just outside of the vortex (dotted triangle) following the main flow. Before and after the red region along the main flow, negative correlations (blue color) were also observed because if clustering occurs, particle depletion follows in the region before and after as a reaction of cluster formation. As a result, the vortex size can be estimated by observing the particle clusters that pass by the vortex to the contraction entry.
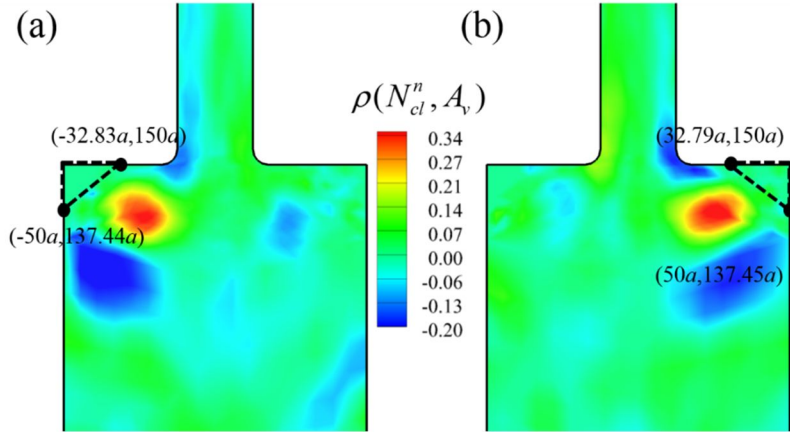
Fig. 4.9. Pearson's correlation coefficients between cluster size N_{cl} and vortex size A_v: (a) left corner and (b) right corner on x-z plane at the center plane (y=0); dashed triangle indicates the average vortex size.

Chapter 5. Concluding remarks

Firstly, we investigated the dynamics of short dsDNA separation in a nanofilter channel with the rigid-rod Brownian dynamics simulation method and introduced a new mechanism for the constraint effect in a high-throughput regime. In the right angle channel, an Ogston-sieving type motion in low Pe^b and a reverse order in high Pe^b was reproduced. In the high Pe^b regime, the constraint effect was found to be a key factor for the filtration process in the nanofilter channel. Due to the constraint effect, there was lateral shift of the rigid-rod molecule, which was rod-length dependent. The laterally shifted molecule translated deterministically in a deep well. In addition, the geometry effect on the nanofilter process was analyzed by changing the tapering angle of a nanofilter channel. Ogston-sieving mechanism was dominant in the low Pe^b regime, and the reverse order tendency was found in the high Pe^b regime. At this high Pe^b regime, the

constraint effect was also studied to explain the higher mobility of larger molecules in a more tapered channel. The findings prove that the constraint effect and deterministic lateral displacement play a key role in the high-throughput nanofilter process and provide a guideline for designing further efficient nanofilter channels to enhance DNA separation performance within the high-throughput regime.

Secondly, in order to understand the characteristics of these complex flows more in depth, we applied Self-consistent particle simulation method to three dimensional 4:1 planar contraction flow of aggregating particle system. Formation of heterogeneous cluster was observed and the flow of particle systems showed spatio-temporal fluctuation. The flow characteristics changed with time and position as the particles flow into the channel. The degree of temporal fluctuation of the velocity field was heterogeneous such that the fluctuation was large at the center of contraction entry and the fluctuation of pressure was large at the corner of contraction entry. In contraction entry region, the cluster size was related with the aggregating force, and similar behavior was observed with vortex size and pressure drop, which means that the clustering of the particles practically dominates the complex flow in this case. The fluctuations in vortex size and cluster size were also dependent on the position of the particle cluster. The size of the

clusters that pass by outside of the vortex along the main flow direction significantly affected the fluctuation of vortex size.

The results about particulate systems in confined microchannel flow help us understand the physics of the flow of complex fluids such as colloid, particle, droplet and biomass, and contribute to support the experiments in understanding the real processes of complex flow field.

Bibliography

In alphabetical order by first author,

Austin, R. H.; Volkmuth, W. D., Electrophoresis and Microlithography, Analusis, 21, 235-238, **1993**.

Bakajin, O.; Duke, T. A. J.; Tegenfeldt, J., Chou, C. F.; Chan, S. S.; Austin, R. H.; Cox, E. C., Separation of 100-kilobase DNA molecules in 10 seconds, Anal Chem, 73, 6053-6056, **2001**.

Berg, H. C., Random Walks in Biology, Princeton University Press, Princeton, **1993**.

Berne, B. J.; Pecora, R., Dynamic Light Scattering, Wiley, New York, **1976**.

Bernate, J.A.; Drazer, G., Stochastic and Deterministic Vector Chromatography of Suspended Particles in One-Dimensional Periodic Potentials, Phys Rev Lett, 108, **2012**.

Broersma, S., Rotational Diffusion Constant of a Cylindrical Particle, J Chem   Phys, 32, 1626-1631, **1960**.

Broersma, S., Viscous Force Constant for a Closed Cylinder, J Chem Phys, 32,   1632-1635, **1960**.

Brady, J.F.; Bossis, G., Stokesian Dynamics, Annual Review of Fluid Mechanics, 20, 111-157, **1988**.

Chen, L.B.; Chow, M.K.; Ackerson, B.J.; Zukoski, C.F., Rheological and Microstructural Transitions in Colloidal Crystals, Langmuir, 10, 2817-2829, **1994**.

Crochet, M.J.; Davies, A.R.; Walters, K., Numerical simulation of non-Newtonian flow, Elsevier, Amsterdam, **1984**.

Desreumaux, N.; Caussin, J.B.; Jeanneret, R.; Lauga, E.; Bartolo, D., Hydrodynamic Fluctuations in Confined Particle-Laden Fluids, Phys Rev Lett, 111, **2013**.

Dorfman, K. D., DNA electrophoresis in microfabricated devices, Rev Mod Phys, 82, 2903-2947, **2010**.

Dorfman, K. D.; King, S. B.; Olson, D. W.; Thomas, J. D. P.; Tree, D. R., Beyond Gel Electrophoresis: Microfluidic Separations, Fluorescence Burst Analysis, and DNA Stretching, Chem Rev, 113, 2584-2667, **2013**.

Doyle, P. S.; Bibette, J.; Bancaud, A.; Viovy, J. L., Self-assembled magnetic matrices for DNA separation chips, Science, 295, 2237-2237, **2002**.

Duke, T. A. J.; Austin, R. H., Microfabricated sieve for the continuous sorting of macromolecules, Phys Rev Lett, 80, 1552-1555, **1998**.

Duong-Hong, D.; Han, J.; Wang, J. S.; Hadjiconstantinou, N. G.; Chen, Y. Z.; Liu, G. R., Realistic simulations of combined DNA electrophoretic

flow and EOF in nano-fluidic devices, Electrophoresis, 29, 4880-4886, **2008**.

Fayad, G. N.; Hadjiconstantinou, N. G., Realistic Brownian Dynamics simulations of biological molecule separation in nanofluidic devices, Microfluid Nanofluid, 8, 521-529, **2010**.

Feigl, K.; Ottinger, H.C., The Flow of a Ldpe Melt through an Axisymmetrical   Contraction - a Numerical Study and Comparison to Experimental   Results, J Rheol, 38, 847-874, **1994**.

Foss, D.R.; Brady, J.F., Brownian Dynamics simulation of hard-sphere colloidal dispersions, J Rheol, 44, 629-651, **2000**.

Foss, D.R.; Brady, J.F., Structure, diffusion and rheology of Brownian suspensions by Stokesian Dynamics simulation, J Fluid Mech, 407, 167-200, **2000**.

Fu, J. P.; Mao, P.; Han, J. Y., Nanofilter array chip for fast gel-free

biomolecule   separation, Appl Phys Lett, 87, 263902, **2005**.

Fu, J. P.; Schoch, R. B.; Stevens, A. L.; Tannenbaum, S. R.; Han, J. Y., Molecular sieving in periodic free-energy landscapes created by patterned nanofilter arrays, Nat Nanotechnol, 2, 121-128, **2007**.

Fu, J. P.; Yoo, J.; Han, J. Y., Molecular sieving in periodic free-energy landscapes created by patterned nanofilter arrays, Phys Rev Lett, 97, 018103, **2006**.

Gachelin, J.; Mino, G.; Berthet, H.; Lindner, A.; Rousselet, A.; Clement, E., Non-Newtonian Viscosity of Escherichia coli Suspensions, Phys Rev Lett, 110, **2013**.

Grassia, P.S.; Hinch, E.J.; Nitsche, L.C.;, Computer-Simulations of Brownian-
Motion of Complex-Systems, J Fluid Mech, 282, 373-403, **1995**.

Han, J.; Turner, S. W.; Craighead, H. G., Entropic trapping and escape of long   DNA molecules at submicron size constriction, Phys Rev Lett, 83,

1688-1691, **1999**.

Hulsen, M.A.; vanHeel, A.P.G.; vandenBrule, B.H.A.A., Simulation of viscoelastic flows using Brownian configuration fields, J Non-Newton Fluid, 70, 79-101, **1997**.

Huang, L. R.; Cox, E. C.; Austin, R. H.; Sturm, J. C., Continuous particle separation through deterministic lateral displacement, Science, 304, 987-990, **2004**.

Isa, L.; Besseling, R.; Morozov, A.N.; Poon, W.C.K., Velocity Oscillations in Microfluidic Flows of Concentrated Colloidal Suspensions, Phys Rev Lett, 102, **2009**.

Karlsson, R.; Karlsson, M.; Karlsson, A.; Cans, A.S.; Bergenholtz, J.; Akerman, B.; Ewing, A.G.; Voinova, M.; Orwar, O., Moving-wall-driven flows in nanofluidic systems, Langmuir, 18, 4186-4190, **2002**.

Kim, J.M.; Chung, C.; Ahn, K.H.; Lee, S.J.; Time-weissenberg number superposition in 4 : 1 planar contraction flow of a viscoelastic fluid, Nihon Reoroji Gakk, 33, 191-197, **2005**.

Kim, J.M.; Doyle, P.S., A Brownian dynamics-finite element method for simulating DNA electrophoresis in nonhomogeneous electric fields, J Chem Phys, 125, **2006**.

Kwon, Y., Numerical description of elastic flow instability and its dependence on liquid viscoelasticity in planar contraction, J Rheol, 56, 1335-1362, **2012**.

Laachi, N.; Declet, C.; Matson, C.; Dorfman, K. D., Nonequilibrium transport of rigid macromolecules in periodically constricted geometries, Phys Rev Lett, 98, 098106, **2007**.

Laso, M.; Ottinger, H.C., Calculation of Viscoelastic Flow Using Molecular-Models - the Connffessit Approach, J Non-Newton Fluid, 47, 1-20, **1993**.

Li, Z. R.; Liu, G. R.; Chen, Y. Z.; Wang, J. S.; Bow, H.; Cheng, Y.; Han, J. Y., Continuum transport model of Ogston sieving in patterned nanofilter arrays for separation of rod-like biomolecules, Electrophoresis, 29,

329-339, **2008**.

Loose, W.; Ackerson, B.J., Model-Calculations for the Analysis of Scattering Data from Layered Structures, J Chem Phys, 101, 7211-7220, **1994**.

Mckinley, G.H.; Raiford, W.P.; Brown, R.A.; Armstrong, R.C., Nonlinear Dynamics of Viscoelastic Flow in Axisymmetrical Abrupt Contractions, J Fluid Mech, 223, 411-456, **1991**.

Meinhardt, S.; Smiatek, J.; Eichhorn, R.; Schmid, F., Separation of Chiral Particles in Micro- or Nanofluidic Channels, Phys Rev Lett, 108, **2012**.

Minc, N.; Futterer, C.; Dorfman, K. D.; Bancaud, A.; Gosse, C.; Goubault, C.; Viovy, J. L., Quantitative microfluidic separation of DNA in self-assembled magnetic matrixesAnal Chem, 76, 3770-3776, **2004**.

Mitchell, P.J.; Heyes, D.M.; Melrose, J.R., Brownian-Dynamics Simulations of Model Stabilized Colloidal Dispersions under Shear, J Chem Soc Faraday T, 91, 1975-1989, **1995**.

Myung, J.S.; Song, S.; Ahn, K.H., Dynamics of model-stabilized colloidal suspensions in confined Couette flow, J Non-Newton Fluid, 199, 29-36, **2013**.

Myung, J.S.; Song, S.; Ahn, K.H.; Lee, S.J., Self-consistent particle simulation   of model-stabilized colloidal suspensions, J Non-Newton Fluid, 166,   1183-1189, **2011**.

Newman, J.; Swinney, H. L.; Day, L. A., Hydrodynamic Properties and Structure of Fd Virus, J Mol Biol, 116, 593-603, **1977**.

Nguyen, H.; Boger, D.V., Kinematics and Stability of Die Entry Flows, J Non-   Newton Fluid, 5, 353-368, **1979**.

Nixon, G. I.; Slater, G. W., DNA Electrophoretic Collisions with Single Obstacles, Phys Rev E, 50, 5033-5038, **1994**.

Öttinger, H. C., Stochastic processes in polymeric fluids: Tools and examples

for developing simulation algorithms, Springer, Berlin, **1996**.

Pan, W.X.; Caswell, B.; Karniadakis, G.E., Rheology, Microstructure and Migration in Brownian Colloidal Suspensions, Langmuir, 26, 133-142, **2010**.

Reguera, D.; Luque, A.; Burada, P.S.; Schmid, G.; Rubi, J.M.; Hanggi, P., Entropic Splitter for Particle Separation, Phys Rev Lett, 108, **2012**.

Royall, C.P.; Dzubiella, J.; Schmidt, M.; van Blaaderen, A., Nonequilibrium sedimentation of colloids on the particle scale, Phys Rev Lett, 98, **2007**.

Schwierz, N.; Nielaba, P., Colloidal systems in three-dimensional microchannels: Lattice control via channel width and external force, Phys Rev E, 82, **2010**.

Sengupta, A.; Tkalec, U.; Ravnik, M.; Yeomans, J.M.; Bahr, C.; Herminghaus, S., Liquid Crystal Microfluidics for Tunable Flow Shaping, Phys Rev Lett, 110, **2013**.

Sevick, E. M.; Williams, D. R. M., Motion of a Polyelectrolyte Chain Hooked   around a Post, Phys Rev E, 50, R3357-R3360, **1994**.

Sevick, E. M.; Williams, D. R. M., Collision of a field-driven polymer with a
    post: Electrophoresis in microlithographic arrays, Phys Rev Lett, 76,
    2595-2598, **1996**.

Saville, P. M.; Sevick, E. M., Collision of a field-driven polymer with a
finite-   sized obstacle: A Brownian dynamics simulation, Macromolecules,
    32, 892-899, **1999**.

Somasi, M.; Khomami, B.; Woo, N. J.; Hur, J. S.; Shaqfeh, E. S. G.,
Brownian   dynamics simulations of bead-rod and bead-spring chains:
numerical   algorithms and coarse-graining issues, J Non-Newton Fluid,
108, 227-   255, **2002**.

Shereda, L.T.; Larson, R.G.; Solomon, M.J., Shear banding in crystallizing
    colloidal suspensions, Korea-Aust Rheol J, 22, 309-316, **2010**.

Shereda, L.T.; Larson, R.G.; Solomon, M.J., Boundary-Driven Colloidal

Crystallization in Simple Shear Flow, Phys Rev Lett, 105, **2010**.

Stancik, E.J.; Hawkinson, A.L.; Vermant, J.; Fuller, G.G., Dynamic

transitions   and oscillatory melting of a two-dimensional crystal

subjected to   shear flow, J Rheol, 48, 159-173, **2004**.

Strating, P., Brownian dynamics simulation of a hard-sphere suspension,

Phys   Rev E, 59, 2175-2187, **1999**.

Streek, M.; Schmid, F.; Duong, T. T.; Ros, A., Mechanisms of DNA

separation   in entropic trap arrays: a Brownian dynamics simulation, J

Biotechnol,   112, 79-89, **2004**.

Strychalski, E. A.; Lau, H. W.; Archer, L. A., Nonequilibrium separation of

short DNA using nanoslit arrays, J Appl Phys, 106, 024915, **2009**.

Utz, M.; Landers, J., Magnetic Resonance and Microfluidics, Science, 330,

1056-1058, **2010**.

Viovy, J. L., Electrophoresis of DNA and other polyelectrolytes: Physical mechanisms, Rev Mod Phys, 72, 813-872, **2000**.

Volkmuth, W. D.; Duke, T.; Wu, M. C.; Austin, R. H.; Szabo, A., DNA Electrodiffusion in a 2d Array of Posts, Phys Rev Lett, 72, 2117-2120, **1994**.

Wapperom, P.; Keunings, R.; Legat, V., The backward-tracking Lagrangian particle method for transient viscoelastic flows, J Non-Newton Fluid, 91, 273-295, **2000**.

Wootton, R.C.R.; Demello, A.J., MICROFLUIDICS Analog-to-digital drug screening, Nature, 483, 43-44, **2012**.

Wu, Y.L.; Derks, D.; van Blaaderen, A.; Imhof, A.;, Melting and crystallization of colloidal hard-sphere suspensions under shear, P Natl Acad Sci USA, 106, 10564-10569, **2009**.

Yamakawa, H., Modern Theory of Polymer Solutions, Harper and Row, New

York, **1971**.

Zero, K. M.; Pecora, R., Rotational and Translation Diffusion in Semi-Dilute

Solutions of Rigid Rod Macromolecules, Abstr Pap Am Chem S,

181,   45-Poly, **1981**.

국문초록

　　　　제한된 미세유로에서 입자 시스템의 수치모사 연구는
다양한 활용이 가능한 랩온어칩 (lab on a chip) 개발에 있어
매우 중요하며, 이러한 이유로 기초 연구와 응용연구에서 많은
관심을 받아왔다. 우선, 우리는 깊고 얕은 부분이 반복되는 나노
필터 (nanofilter) 를 흘러가는 짧은 이중나선 DNA의 거동을
브라운 거동 수치모사를 이용해 조사하였다. 이를 통해 높은
생산성 영역의 DNA 분류 공정에서 제시된 기존의 연구 (Laachi *et
al.*, Physical Review Letters, 2007, 98) 와 다른 새로운
메커니즘을 제시하였다. 이를 통해 채널 얇은 부분 출구에서
기하학적인 제한에 의해 DNA 분자는 결정론적으로 길이에 따라
다른 전기영동 유선으로 이동하는 것을 보였다. 결과적으로, 긴
DNA분자는 깊은 부분에서 아래쪽으로의 이동이 적은 상태로
이동하였으며, 이는 짧은 분자가 깊은 부분에서 긴 체류시간을

가진 것과 반대되는 현상이다. 우리는 나노 필터에서의 DNA분자의 거동을 전기영동 역학을 통해 설명하였다. DNA분자의 길이에 따른 통계적 위치 분포 차이는 이러한 우리의 가정을 뒷받침하였다. 또한 채널의 얕은 부분과 깊은 부분 사이의 꺾인 각도는 DNA분류 효율에 중요한 역할을 하는 것을 발견하였다. 이는 채널의 모양에 따라 다른 불균일하게 분포된 전기장과 기하학적 제한 모델의 결합된 결과를 보여준다. 이러한 결과들은 나노유로의 DNA분류 장치의 디자인과 활용에 이용될 것이며, 제한된 환경에서 고분자의 거동 특성을 이해하는 데에 도움을 줄 것이라 기대된다.

또한, 제한된 복잡한 형태의 채널에서 복잡 유체의 미세구조의 변화와 유동과의 상호 관계에 대해 조사하였다. 이러한 복잡한 유동의 특성을 이해하기 위해, 우리는 4:1 수축관 유동에서 응집성 입자 서스펜전의 거동을 자기 일관적 입자계 유동해석 기법을 통해 연구하였다. 자기 일관적 입자계 유동해석 기법은 브라운 동력학과 유한 요소법을 자기 일관적으로 결합한 것으로, 긴 영역에서의 수력학을 효율적으로 고려한다. 이를 통해 우리는 위치에 따라 불균일하게 입자 구조체가 형성되는 것을 발견하였고, 이를 유동과 입자 상호력의 경쟁관계로 분석하였다. 또한 미세구조의 변화와 이와 유동과의 상호작용에서 기인한 시간-공간상의 유동 변동을 관찰하였다. 이러한 변동은 매우 복잡하여 주기성이나 패턴 특성이 없었다. 이러한 결과를 통해 불균일 구조 형성과 시공간의 유동특성의 변동은 미세 수축 유로를 흐르는 입자 서스펜전의 복잡한 유동을 특징짓는 주요한 요소가 됨을 알 수 있다.